Contrasting Southern Hemisphere Monsoon Response: MidHolocene Orbital Forcing versus Future Greenhouse Gas–Induced Global Warming

ROBERTA D'AGOSTINO

Max Planck Institute for Meteorology, Hamburg, Germany

JOSEPHINE R. BROWN

School of Earth Sciences, and ARC Centre of Excellence for Climate Extremes, University of Melbourne, Melbourne, Victoria, Australia

AUREL MOISE AND HANH NGUYEN

Bureau of Meteorology, Melbourne, Victoria, Australia

PEDRO L. SILVA DIAS

Institute of Astronomy, Geophysics and Atmospheric Sciences, University of São Paulo, São Paulo, Brazil

JOHANN JUNGCLAUS

Max Planck Institute for Meteorology, Hamburg, Germany

(Manuscript received 10 September 2019, in final form 8 July 2020)

ABSTRACT

Past changes of Southern Hemisphere (SH) monsoons are less investigated than their northern counterpart because of relatively scarce paleodata. In addition, projections of SH monsoons are less robust than in the Northern Hemisphere. Here, we use an energetic framework to shed lights on the mechanisms determining SH monsoonal response to external forcing: precession change at the mid-Holocene versus future greenhouse gas increase (RCP8.5). Mechanisms explaining the monsoon response are investigated by decomposing the moisture budget in thermodynamic and dynamic components. SH monsoons weaken and contract in the multimodel mean of midHolocene simulations as a result of decreased net energy input and weakening of the dynamic component. In contrast, SH monsoons strengthen and expand in the RCP8.5 multimodel mean, as a result of increased net energy input and strengthening of the thermodynamic component. However, important regional differences on monsoonal precipitation emerge from the local response of Hadley and Walker circulations. In the midHolocene, the combined effect of Walker–Hadley changes explains the land–ocean precipitation contrast. Conversely, the increased local gross moist stability explains the increased local precipitation and net energy input under circulation weakening in RCP8.5.

1. Introduction

Phase 5 of the Coupled Model Intercomparison Project (CMIP5) models simulate more realistically monsoon climatology and variability than their predecessors, phase 3 of CMIP (CMIP3). Factors that have contributed to the improved representation include better simulation of topography-related monsoon precipitation because of higher horizontal resolution (Mizuta et al. 2012), improved propagation of intraseasonal variations (Sperber et al. 2013), and a more realistic simulation of El Niño–Southern Oscillation (ENSO) monsoon teleconnection (Meehl et al. 2012). Challenges remain for the simulation of monsoons in both Northern and Southern Hemispheres (NH and SH), including the complexity of the land–ocean–atmosphere interactions coupled to tropical–extratropical

Denotes content that is immediately available upon publication as open access.

Corresponding author: Roberta D'Agostino, roberta.dagostino@mpimet.mpg.de

DOI: 10.1175/JCLI-D-19-0672.1

climate phenomena (e.g., ENSO and Madden–Julian oscillation, Indian and Atlantic SST variability, Hadley and Walker circulations, and extratropical cyclones) (Mohtadi et al. 2016).

The last Intergovernmental Panel on Climate Change AR5 projected an increased area and intensity of the global monsoon (i.e., the aggregation of all monsoon systems) in the twenty-first century and a robust tropical atmospheric circulation weakening (Christensen et al. 2013) associated with reinforcement of low-level moisture convergence (Hsu et al. 2012; Kitoh et al. 2013; Lee and Wang 2014). However, model skill in representing regional monsoons is lower compared to the global monsoon and varies across different monsoon systems.

In the NH, CMIP3 and CMIP5 simulations have indicated a consistent wettening tendency of the Asian monsoon at the end of the twenty-first century (Kitoh et al. 2013; Endo and Kitoh 2014), but they have shown poor intermodel agreement on West African monsoon response because of the competing effects of CO_2 increase and SST warming (Biasutti 2013; Gaetani et al. 2017). Also, projections of the North American monsoon remain inconclusive with most models projecting a delay in the monsoon season but no robust changes in its summer mean intensity (Cook and Seager 2013; Seth et al. 2013, 2011; Pascale et al. 2019).

In the SH, projections of the Australian monsoon under high emissions based on CMIP5 models indicate a moderate increase or little change, with low confidence, at the end of the twenty-first century (Jourdain et al. 2013; Brown et al. 2016). Projections of the South American monsoon show an overall increased precipitation over southern Brazil, Uruguay, and northern Argentina (Jones and Carvalho 2013) and a slight decrease in the Amazon (low confidence; Boisier et al. 2015). However, an expansion of the South American monsoon area is projected with high confidence (Endo and Kitoh 2014). Projected rainfall change in the South and East African monsoon also has low confidence (Christensen et al. 2013; Pascale et al. 2019).

Recent works on moisture budget decomposition (Endo and Kitoh 2014; D'Agostino et al. 2019) showed that the wettening tendency in NH monsoons is due to specific humidity increase under future warming. In contrast, in the SH, projected rainfall change in the multimodel ensemble mean at the end of the twenty-first century shows no robust signal (Seager et al. 2003; Endo and Kitoh 2014; Brown et al. 2016).

Important steps forward to better understand the complex response of monsoons to climate change have been made by linking the tropical rainfall and atmospheric circulation response to the net energy input (NEI) change (Biasutti et al. 2018; D'Agostino et al. 2019). Analysis of the energy budget applied to the global mean precipitation may provide further insights into what controls regional rainfall changes (Levermann et al. 2009; Muller and O'Gorman 2011; O'Gorman et al. 2012). In this framework, zonal-mean tropical precipitation and the intertropical convergence zone (ITCZ) are parts of the mean meridional circulation (Donohoe 2016), which is expected to shift off the equator, into the hemisphere where the atmosphere is heated more strongly (Schneider et al. 2014).

As fundamental components of the tropical overturning, monsoons are viewed as moist energetically direct circulations tightly connected to the Hadley circulation (Bordoni and Schneider 2008; Schneider et al. 2014; Biasutti et al. 2018). They act to export moist static energy (MSE) away from their ascending branches and precipitation maxima. If vertically integrated eddy MSE flux is negligible, the NEI flux into the atmospheric column, given by the difference between top-of-atmosphere radiative and surface energy fluxes, is primarily balanced by divergence of vertically integrated MSE flux due to the mean flow in a steady state, which is describing $P - E$ change in the tropics (Neelin and Held 1987; Chou et al. 2001; Merlis et al. 2013; Boos and Korty 2016). In particular, Muller and O'Gorman (2011) argue that changes in radiative and surface sensible heat fluxes provide a guide to the local precipitation response over land. Therefore, any changes in NEI (e.g., related to precession-induced insolation changes, aerosols, greenhouse gases, and others) require anomalous energy transport to restore the energy balance. Given that, during the summer, most of this transport is carried out by monsoonal circulations (Heaviside and Czaja 2013; Walker 2017), this would imply a shift of the monsoonal circulation ascending branches and precipitation maxima into the hemisphere with increased NEI and, possibly, an associated meridional atmospheric circulation strengthening (Schneider et al. 2014; Bischoff et al. 2017). The degree to which changes in energy transport implied by a given radiative forcing are accomplished through just changes in circulation strength or changes in energy stratification (or gross moist stability; Neelin and Held 1987) is still debated.

To better understand SH monsoon dynamics despite model uncertainty and to improve our understanding on the relationship between energy and precipitation already found in the NH (D'Agostino et al. 2019), we have been investigated SH monsoon changes in three experiments that show very different spatial distribution of the NEI: midHolocene, preindustrial control (piControl), and RCP8.5 simulations from the Coupled and Paleoclimate Model Intercomparison Project (PMIP3–CMIP5). The mid-Holocene, a period around 6000 years before present, experienced different seasonality of

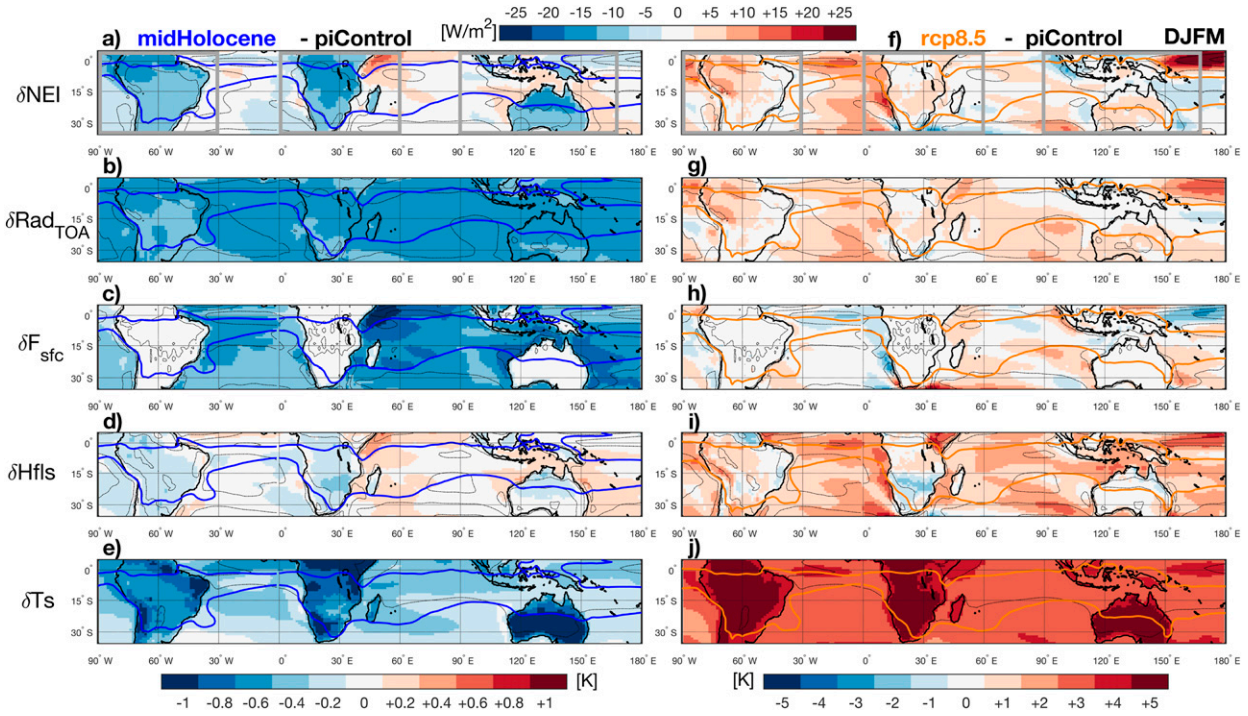

FIG. 1. Differences in NEI, top-of-atmosphere radiative fluxes (Rad_{toa}), surface fluxes (F_{sfc}), latent heat flux (Hfls), and skin temperature (Ts) between (a)–(e) the midHolocene and (f)–(j) RCP8.5 relative to piControl in DJFM ensemble means (shading). Only areas where two-thirds of models agree on the sign of the change are shown. PiControl is also shown as reference (dashed lines spaced by 30 W m^{-2} for fluxes and 30 K for temperature). Orange and blue bold lines show areas within which the annual precipitation range (DJFM minus JJAS) exceeds 2 mm day^{-1} for RCP8.5 and midHolocene, respectively.

insolation relative to the present day in each hemisphere. The associated warming is expected to drive shifts in the timing and intensity of regional monsoons, resembling future global warming RCP8.5 scenario in the NH. However, the midHolocene and RCP8.5 show very different structure of the NEI (Fig. 1) because they are driven by very different forcing (i.e., orbital changes vs greenhouse gas increase). Therefore, they are useful to analyze differences and similarities of past and future monsoons. The most important forcing of the midHolocene experiment is the insolation change associated with different orbital parameters compared to present day. The effect of precession is the increased (decreased) seasonality in the NH (SH) and an enhanced NEI contrast between land and ocean. On the other hand, the RCP8.5 scenario is mainly driven by greenhouse gas concentration increase during the twenty-first century. Increased opacity of the atmosphere to thermal radiation results in a spatially homogeneous increase of the top-of-atmosphere radiation imbalance (Lembo et al. 2019). Given the fact that precipitation minus evaporation ($P - E$) and atmospheric circulation must respond to NEI forcing into the air column, monsoons are stronger in midHolocene (because of orbital forcing) and in RCP8.5 simulations (because of enhanced greenhouse gas effect) in the NH boreal summer compared to preindustrial conditions (D'Agostino et al. 2019). However, while NH monsoons are widely investigated in model simulations and reconstructions of the mid-Holocene (Liu and Ding 1998; Schulz et al. 1998; Haug et al. 2001; Fleitmann et al. 2003; Yuan et al. 2004; Zhao et al. 2005; Weldeab et al. 2007; Tjallingii et al. 2008; Wang et al. 2008; Lézine et al. 2011; Zhao and Harrison 2012; Hély and Lézine 2014; Tierney and Pausata 2017), little attention has been paid to the SH counterpart, where conflicting information from paleodata highlights the need to better understand SH monsoon dynamics for both past and future climates.

A recent multiproxy paleodata synthesis of the mid-Holocene vegetation changes across SH tropical South America show increased savannah/grassland cover consistent with drier than present-day conditions in South America, linked to a weaker monsoon (Smith and Mayle 2018). In contrast, northeastern Brazil's climate is out of phase with the rest of tropical South America (Cruz et al. 2009; Smith and Mayle 2018), suggesting different mechanisms responsible for subregional precipitation changes.

A recent compilation of multiproxy terrestrial and marine records spanning along South Africa shows good agreement with the PMIP3 multimodel mean on both the sign of rainfall change and on the north–south dipole in the mid-Holocene precipitation pattern associated with increased (decreased) insolation in the NH (SH) (Chevalier et al. 2017).

Based on speleothem records from the Kimberley, Western Australia, in northwest Australia, relatively wet conditions have been found in northern Australia in the mid-Holocene [7.5–4.5 thousand years before present (kya)] followed by a drier period around 5.5–6.5 kya (Denniston et al. 2013). Increased aridity from 6.3 to 4.5 kya was also found in pollen and sediment records from northwest Australia (McGowan et al. 2012). Ocean sediment records from the Maritime Continent also indicate relatively dry conditions during the early and mid-Holocene (Mohtadi et al. 2011). However, other records support increased rainfall in northern Australia (Johnson et al. 1999; Magee et al. 2004) and an expansion of rain forest across the Australian tropics (Shulmeister 1999; Rowe 2007). The apparent disagreement between models and some proxy records of northern Australian monsoon rainfall in the mid-Holocene may be partly due to the spatial complexity of the response, with evidence of past shifts in both the position and extent of the tropical convergence zone in the Indo-Pacific region (Mohtadi et al. 2011; Denniston et al. 2013; Krause et al. 2019).

Shedding light on the complex dynamics of SH monsoons is therefore important not only to improve our understanding of the phenomenon in the future climate, but also to improve our interpretation of proxy reconstructions. Additionally, the comparison of past and future changes in the SH monsoon provides insights into the sensitivity of regional monsoons to changes in the mean state, including seasonal changes in temperature (due to either insolation or greenhouse gas forcing) and changes in the relative heating of land and ocean. While past and future forcings differ, understanding of the underlying mechanisms driving changes in the SH monsoons can be obtained from comparing these two cases.

2. Data and methods

We make use of midHolocene, piControl, and RCP8.5 experiments that are available in the CMIP5 archives. We use the first ensemble member (r1i1p1) of nine models with all three experiments available (i.e., BCC_CSM1.1, CCSM4, CNRM-CM5, CSIRO Mk3.6.0, FGOALS-g2, HadGEM2-ES, IPSL-CM5A-LR, MIROC-ESM, and MRI-CGCM3). All datasets are interpolated to a common $1° \times 1.25°$ latitude/longitude grid and to 17 pressure levels.

MidHolocene and RCP8.5 are two experiments that show very different spatial distribution of the NEI, hence they might be useful, altogether piControl used here as reference, to expand the ongoing debate on the relationship between energy and precipitation.

December–March (DJFM) climatologies are calculated for the last 30 years of RCP8.5, for the period 1850–2005 of piControl and for the last 100 years of midHolocene simulations.

Changes in monsoon extent and strength are assessed using the following metrics: the monsoon extent is the land-only area where annual precipitation range, defined as the difference between summer and winter rainfall, exceeds 2 mm day^{-1} for each monsoon domain. The selected threshold defines a concentrated summer rainy season and distinguishes monsoons from year-round rainy regimes (Zhou et al. 2008; Liu et al. 2009; Hsu et al. 2012). Choosing different definitions to calculate land-monsoon area (e.g., local summer precipitation exceeding 35%, 40%, 50% of the annual rainfall) does not significantly affect our results. The monsoon strength is the average summer land rainfall calculated in each monsoon domain as previously defined (see colored curves in Fig. 1) within each of the following boxes (see Fig. 1):

1) South American monsoon (SAM),
2) South African monsoon (SAF), and
3) Australian monsoon (AUS).

We also consider the entire SH tropical land-monsoon area (0°–35°S, 0°–360°E) based on the same definition of monsoon areas given above.

Following Trenberth and Guillemot (1995), the linearized anomalous moisture budget is decomposed into thermodynamic and dynamic components and a residual (Res) as

$$\rho_w g \delta(\overline{P} - \overline{E}) = -\int_0^{p_s} \nabla \cdot (\delta \overline{q}\, \overline{\mathbf{u}}_{\text{piControl}})\, dp + \\ -\int_0^{p_s} \nabla \cdot (\overline{q}_{\text{piControl}} \delta \overline{\mathbf{u}})\, dp - \text{Res}, \quad (1)$$

where overbars indicate time means, $(P - E)$ is precipitation minus evaporation, p is pressure, p_s is surface pressure, q is specific humidity, $\overline{\mathbf{u}}$ is the horizontal wind, and ρ_w is the water density; δ is the departure from the reference climate (piControl).

On the right-hand side of Eq. (1), the first term is the thermodynamic contribution (TH) to the moisture budget: it represents changes in moisture flux convergence arising from changes in moisture, which generally follow the Clausius–Clapeyron relation for negligible relative humidity changes (e.g., Held and Soden 2006).

The second term is the dynamic contribution (DY): it involves changes in winds with unchanged moisture and is mostly related to changes in the mean atmospheric flow. Res accounts for transient eddy (TE) contribution (including nonlinear terms, which are generally negligible) and surface (S). Figures showing the intermodel spread of these quantities are included in appendix A, and further details on the method are described in appendix B.

All these quantities are evaluated by averaging TH, DY, and Res terms in each monsoon domain, considering only land values within each colored curve and within each box shown in Fig. 1.

Following Neelin and Held [1987, their Eq. (2.5)], the column-integrated MSE budget is balancing the top-to-bottom energy fluxes (i.e., the NEI):

$$\left\{\frac{\partial \overline{h}}{\partial t}\right\} + \{\nabla \cdot \overline{\mathbf{u}}\,\overline{h}\} + \{\nabla \cdot \overline{\mathbf{u}'h'}\} = \overline{\mathrm{NEI}}, \qquad (2)$$

where $\{\partial\overline{h}/\partial t\}$ is the vertically integrated MSE tendency, $\{\nabla \cdot \overline{\mathbf{u}}\,\overline{h}\}$ is the vertically integrated MSE flux due to the mean flow, $\{\nabla \cdot \overline{\mathbf{u}'h'}\}$ is the vertically integrated eddy MSE flux, and NEI is the net energy input defined as $\mathrm{Rad_{TOA}} - F_{\mathrm{sfc}}$, where $\mathrm{Rad_{TOA}}$ is the net top-of-atmosphere radiative fluxes, and F_{sfc} is the sum of the surface radiative and turbulent fluxes (latent and sensible).

However, in steady state and in monsoonal regions where eddy MSE flux is small, any anomalous NEI will require changes in MSE export by the mean circulation. The steady state assumption in Eq. (2) holds for long-time integration. Here on seasonal scales we verified that the tendency term neglected in Eq. (2) is smaller than 5% of the total NEI term (not shown).

In this study, we leverage on the energetic framework because its relationship with MSE, although this approach is not formally related to $(P - E)$. This link is, however, helpful for explaining monsoonal changes through moisture budget decomposition and shedding lights on the role played by shifts in the meridional and zonal atmospheric overturning circulation on monsoonal precipitation change. This is done by computing the regional mass streamfunction in the meridional and zonal plane, depicting the Hadley and Walker circulations, respectively, and described in appendix C.

3. Results on SH monsoon: General characteristics

Different responses of monsoonal rainfall over land and ocean are related to the NEI and associated changes in moisture convergence (Hsu et al. 2010). Figure 1 highlights the different spatial pattern and sign of NEI anomalies in the midHolocene and RCP8.5 relative to piControl. The NEI is characterized by a pronounced land–sea contrast in the midHolocene (Fig. 1a), whereas it is largely positive over both land and tropical ocean in RCP8.5, with some regional differences at ocean basin scale (Fig. 1f). The midHolocene anomalous negative NEI over land results from a substantial decrease in incoming solar radiation at the top of the atmosphere associated with orbital forcing in DJFM (Fig. 1b). However, over the ocean the positive anomalies, for example, over the Arabian Sea (Fig. 1a), are mainly due to anomalous turbulent fluxes going out from the ocean (source) into the atmosphere (sink). A decomposition into latent and sensible heat flux indicates a dominance of the latent heat flux term (Fig. 1d). The contrasting response over land and ocean to midHolocene insolation has been assessed in previous studies using either mixed layer or dynamical ocean components (Braconnot et al. 2000, 2007; Ohgaito and Abe-Ouchi 2007; Hsu et al. 2010). Hsu et al. (2010) suggested that the land–sea asymmetry, which occurs particularly pronounced in Austral summer, as memory effect. The ocean responds with a delay to radiative anomalies and remembers the previous season's forcing anomaly of opposite sign, leading to much reduced SST changes over the ocean (Fig. 1e). Conversely, in RCP8.5 the substantial increase of greenhouse-induced opacity of the atmosphere to thermal radiation results in a spatially homogeneous increase of the top-of-atmosphere radiation imbalance (Lembo et al. 2019), reflecting in globally homogeneous NEI, as well as an homogeneous land–sea contrast in the tropical belt and in the SH in DJFM (Fig. 1f). NEI differences at ocean basin scale are primarily related to changes in ocean and atmosphere circulation that lead to flux anomalies at the surface (Figs. 1h,i, respectively): positive anomalies over Atlantic and Pacific equatorial ocean are due to turbulent air–sea fluxes, which are largely uncertain (Fig. A1).

Changes in NEI are related to changes in the horizontal divergence of vertically integrated MSE, which, in a steady state, describes the change in $P - E$ [Eq. (2), Figs. 2a,d]. Given the small contribution of the evaporation to $P - E$ changes (Figs. 2c,f), the balance over land is mainly due to precipitation changes (Figs. 2b,e), which is also the variable that has the strongest intermodel discrepancy (Fig. A2). The homogeneous temperature and energy increase in RCP8.5 (Fig. 1) explains why precipitation increases. Nevertheless, precipitation shows strong regional differences among monsoon domains: Fig. 1 does not show a simple correspondence between anomalous NEI and precipitation patterns, although regionally averaged values have the same sign (Fig. 4). On the other hand, in the midHolocene, precipitation decreases over land, following the simple NEI argument (Fig. 2b).

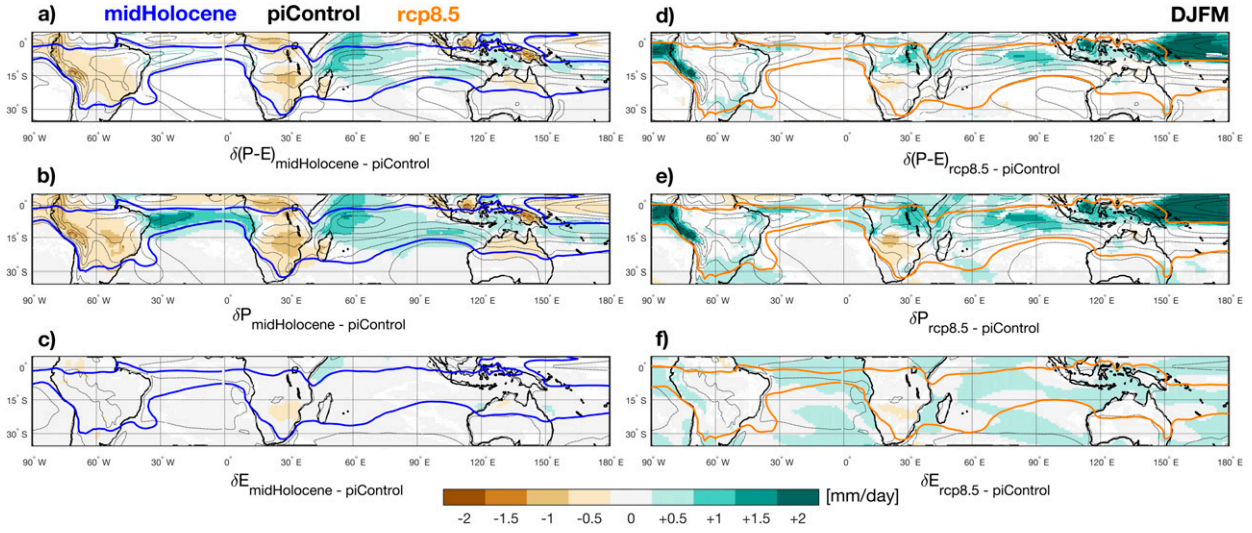

FIG. 2. (a),(d) Precipitation minus evaporation ($P - E$), (b),(e) precipitation, and (c),(f) evaporation difference between (left) the midHolocene and (right) the RCP8.5 relative to piControl in DJFM ensemble means (shading). PiControl is also shown as reference (dashed lines spaced by 2 mm day^{-1}). Only areas where two-thirds of models agree on the sign of the change are shown. Orange and blue bold lines show areas within which the annual precipitation range (DJFM minus JJAS) exceeds 2 mm day^{-1} for RCP8.5 and midHolocene, respectively.

To disentangle the relative contribution of the temperature change (wet-get-wetter mechanisms) and the atmospheric circulation changes to the overall moisture anomaly relative to piControl, we decompose the moisture budget into TH and DY components for the two experiments. The former component attributes $P - E$ changes to change in specific humidity only, while the latter to mean flow changes.

Figure 3 shows the TH, DY, and Res components defined in Eq. (1). In the midHolocene, $P - E$ changes are primarily controlled by the DY component over both land and ocean: the DY weakening (strengthening) is associated with negative (positive) $P - E$ over land (ocean) (cf. here Figs. 2a and 3b). In contrast, $P - E$ response is more complex in RCP8.5: the balance is

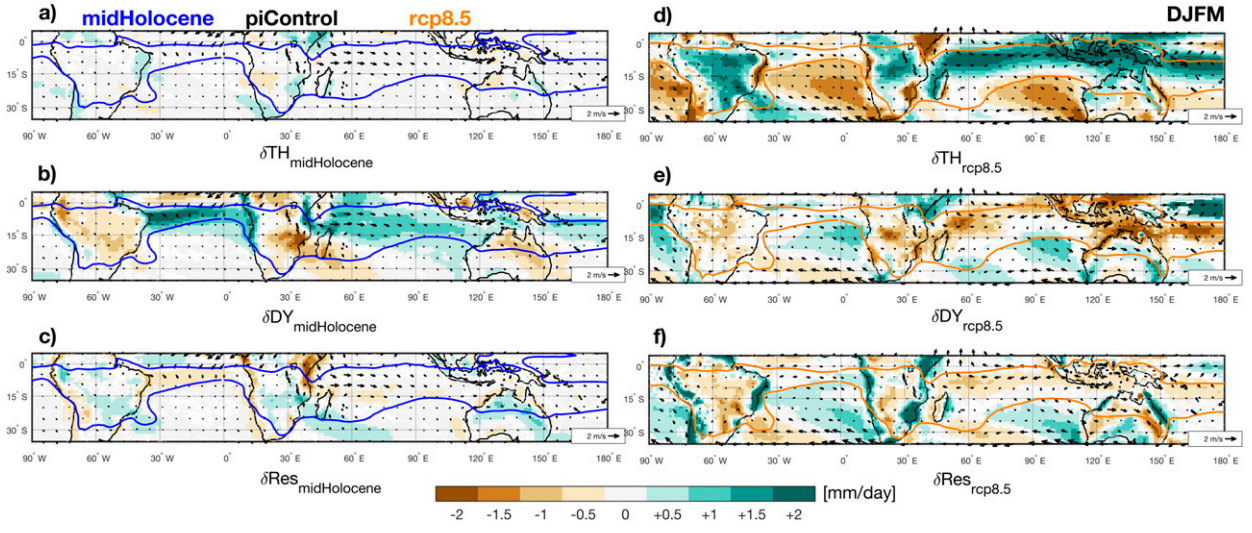

FIG. 3. Changes in ($P - E$) from changes in TH and DY components of the moisture budget for (a),(b) midHolocene and (d),(e) RCP8.5 in DJFM ensemble means (shading). (c),(f) Res for both experiments. Only areas where two-thirds of models agree on the sign of the change are shown. Vectors are 925-hPa wind anomalies for midHolocene and RCP8.5 relative to piControl. Orange and blue bold lines show areas within which the annual precipitation range (DJFM minus JJAS) exceeds 2 mm day^{-1} for RCP8.5 and midHolocene, respectively.

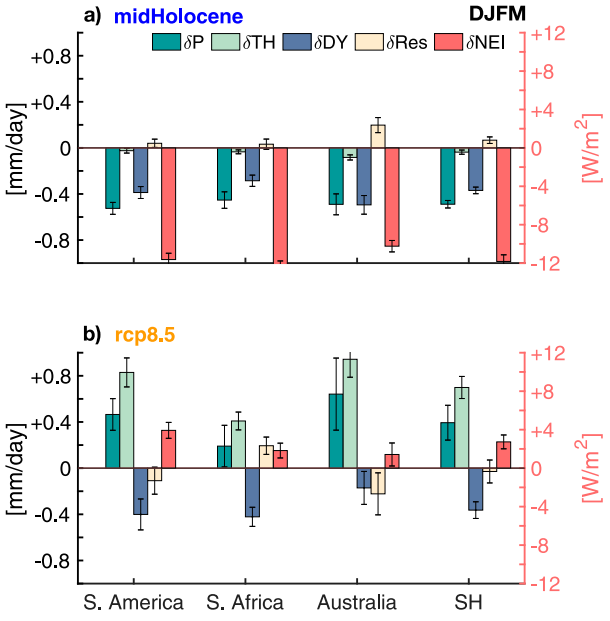

FIG. 4. Regionally averaged (red axis) changes and changes in thermodynamic (δTH) and dynamic (δDY) components of the moisture budget, as well as its residual [δRes; see Eq. (1)] for (a) midHolocene and (b) RCP8.5. Also, the precipitation change relative to piControl is shown for both experiments (δP). Bar ranges indicate the standard error for each contribution computed among the ensemble members.

positive over land and tropical oceans because the TH component is governed by general warming pattern and NEI increase. However, the overall $P - E$ change is counterbalanced by the DY term, which is mainly negative over land, consistent to what has been found in the NH (D'Agostino et al. 2019) and also over the Indian Ocean and in the warm pool region. Consistent with Oueslati et al. (2016) and Tian et al. (2018), we find that the DY weakening is associated with a slowdown of the tropical circulation (Figs. 4, 5). If energy stratification does not change significantly, the slowdown of the tropical circulation implies a weakening of the MSE export from the ascending branches. However, the NEI increase and DY weakening suggests that other factors than the divergence of the mean flow in RCP8.5 must be important for explaining regional monsoonal rainfall change, such as local vertical MSE stratification and/or atmospheric circulation shift (detailed discussion in the following sections). Furthermore, given the nonnegligible contribution of the Res term, especially in RCP8.5, some processes other than mean flow changes, such as transient eddy changes may have a fundamental role in future SH monsoon response (Chadwick et al. 2013; Brown et al. 2016). These features are analyzed in detail for each individual monsoon domain in the following sections.

Applying the energetic framework and the moisture budget decomposition on regional monsoonal rainfall (Fig. 4), the emerging picture is clear for the midHolocene, where it is possible to identify a common behavior among SH monsoons: the overall SH monsoon weakening is associated with atmospheric circulation slowdown (e.g., negative DY change in all monsoon regions and Hadley circulation weakening; Fig. 4), and with a negative NEI over land. In contrast, in RCP8.5 $P - E$ has less uniform response because of the competing effects of the TH and DY terms. In South America and Australia, the positive contribution due to TH increase to the budget is evident. However, the contribution from the Res term is nonnegligible and will be discussed further below. Additionally, the attribution of the overall moisture change to either DY or TH is not possible in South Africa because of the large Res term, where the surface term (Figs. B1, B2) depends strongly on the interpolation procedures over steep orography (Seager et al. 2010) and partially because TH and DY almost cancel each other.

To better address regional variations of TH and DY in light of NEI and circulation changes at ocean basin scale, we analyze and discuss each monsoon separately in the following section.

4. Discussion of local monsoons

a. SAM

The SAM is part of the monsoon system of the Americas and its variability is influenced by a complex interplay of different large-scale and local factors. In the upper troposphere, the summer season is characterized by the presence of the Bolivian high, a feature that has been explained as the response of diabatic local heating in the Amazon region, and a trough over the tropical and subtropical South Atlantic, near the coast of Northeast Brazil (Marengo et al. 2012). On the other hand, low-level features include 1) surface high pressure systems and anticyclonic circulation over the subtropical oceans (Pacific and Atlantic); 2) the Chaco thermal low centered over northern Argentina; 3) the South Atlantic convergence zone (SACZ), a region that extends from the southern Amazonian region to central-eastern South America and the neighboring portion of the Atlantic Ocean, drawing a characteristic quasi-stationary diagonally oriented cloud band region in the northwest–southeast direction (Kodama 1992, 1993); 4) the South American low-level jet east of the Andes, a low-level northwesterly flow east of the Andes that extends from the southwestern Amazon to southeastern South America; 5) the seasonal migration of

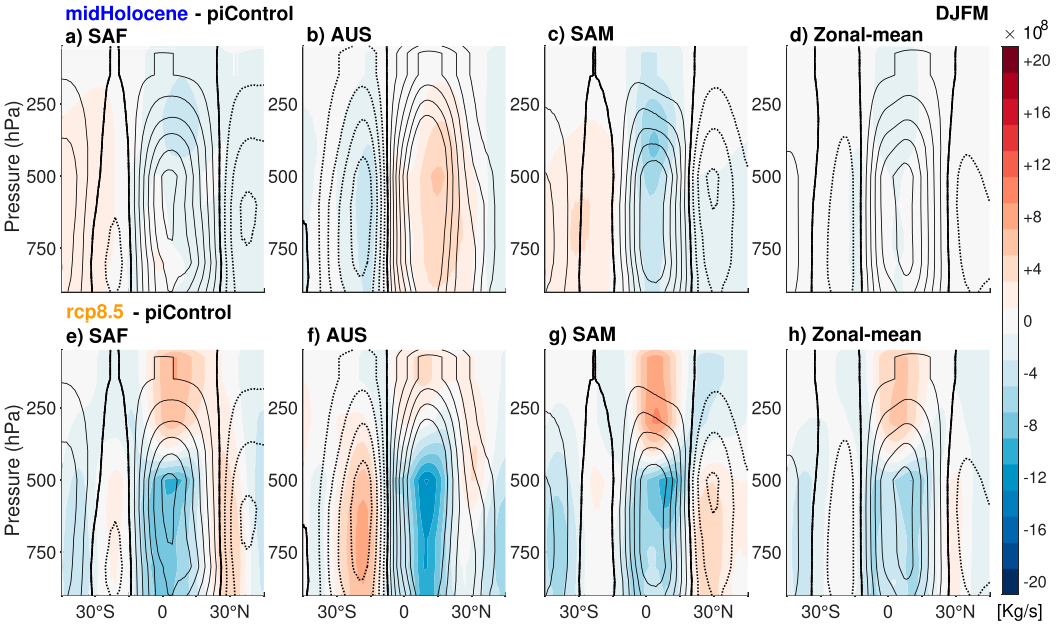

FIG. 5. Multimodel ensemble mean of DJFM local Hadley cell computed in each monsoon domain—SAF, AUS, and SAM—and the zonal mean. Colors show the anomalous circulation in each experiment [(top) midHolocene; (bottom) RCP8.5] relative to piControl. Contours refer to piControl meridional mass streamfunction (contour step is $1 \times 10^9\,\mathrm{kg\,s^{-1}}$). Solid (dotted) lines indicate positive (negative) values of the streamfunction for clockwise (counterclockwise) circulation.

the Atlantic ITCZ over northern South America; and 6) the water recycling in the Amazon.

All of these factors have a different impact on precipitation pattern, therefore the SAM has strong regional variability: for example, the Atlantic ITCZ modulates the northeastern and northern portions of the continent, while the SACZ plays a key role on the precipitation regime of central and southeastern South America, ensuring moisture transport and convective activity from the western Amazon toward southeastern Brazil and the nearby Atlantic Ocean.

Recent SAM indices calculated based on different variables (da Silva and de Carvalho 2007; Raia and Cavalcanti 2008; Nieto-Ferreira et al. 2011; Seth et al. 2010; Kitoh et al. 2013; Endo and Kitoh 2014) all point to medium confidence that local precipitation will remain unchanged in the future.

Our models subset shows a modest strengthening and a slight expansion of SAM monsoon in RCP8.5 ensemble mean relative to piControl (+4.5% and +2.2%, respectively, Table 1), with positive $P - E$ along Northeast Brazilian coasts and over the Andes. The regionally averaged precipitation increase is consistent among models too (Table A1). The positive $P - E$ balance is mainly due to increased precipitation (Fig. 2e). Different mechanisms determine the SAM response to RCP8.5 forcing at subregional scale: models consistently point to the TH component as the most important contribution to the overall moistening of SAM (Figs. 3d, A3d), being largely positive over the Amazon and in the SACZ area. However, TH is counterbalanced by the local DY weakening (Figs. 3e, 4), resulting in small overall $P - E$ changes of the Amazon–central Brazil, consistently with aforementioned studies (Kitoh et al. 2013; Endo and Kitoh 2014). The DY weakening is supported by both weakening of the local Hadley cell (Fig. 5) and South American Walker cell, with an eastward shift of its main updraft (Fig. 6). The main updraft of the local Hadley cell is also deeper: this would indicate a deepening of the convection relative to piControl. Furthermore, other mechanisms are controlling the rainfall response in Northeast Brazil and Brazilian Atlantic coasts, where DY increases similarly to the Atlantic, and where TE and the S are particularly large (see Figs. B1, B2). This highlights the complex subregional features of SAM rainfall.

In the midHolocene ensemble mean, the SAM monsoon slightly contracts and precipitation decreases (−2.1% and −8.5% relative to piControl; Table 1), with 100% of our model agreeing on the sign of regionally averaged values (Table A1). This contraction is consistent with the robust dynamically induced weakening of SH monsoons (Figs. 4, A3). The DY weakening over land is due to the

TABLE 1. Changes in midHolocene and RCP8.5 land-monsoon extent and strength relative to piControl. Standard errors for piControl models are reported in parentheses. The monsoon extent is calculated inside each monsoon domain where the difference between DJFM and JJAS precipitation exceeds 2 mm day^{-1}, as shown in solid lines in Fig. 1.

	Extent (10^6 km^2)			Strength (mm day^{-1})		
Land monsoons	piControl	MidHolocene	RCP8.5	piControl	MidHolocene	RCP8.5
South America	10.3 (±0.3)	−2.1%	+2.2%	6.5 (±0.7)	−8.5%	+4.5%
South Africa	7.7 (±0.3)	−3.6%	+2.8%	5.3 (±0.4)	−7.4%	+3.8%
Australia	3.9 (±0.8)	−13.8%	+6.9%	5.9 (±1.1)	−10.5%	+8.2%
SH	22.0 (±1.2)	−4.7%	+3.3%	6.3 (±0.4)	−7.5%	+4.4%

slowdown of the cross-equatorial Hadley cell in the SAM domain (Fig. 5) and with the increased moisture transport and precipitation toward the Atlantic Ocean, resulting from the shift of South America and Atlantic Walker circulation action centers (Fig. 6). Recent multiproxy paleodata synthesis of the mid-Holocene vegetation changes across SH tropical and subtropical South America show increased savannah/grasslands cover consistent with drier than present-day conditions in South America, linked to a weaker monsoon (Smith and Mayle 2018). In contrast, northeastern Brazil's climate is out of phase with the rest of tropical South America (Cruz et al. 2009; Smith and Mayle 2018). Other studies focused on the equatorial part of the South American monsoon (Wang et al. 2017; Ward et al. 2019) indicate that the ITCZ southward migration throughout the equatorial sector of South America is not consistent with the speleothem data across the continent from Peru to Northeast Brazil. Increased precipitation in Northeast Brazil and the eastern Amazon is coherent with the southward ITCZ migration. However, the observed drying in central part of the Amazon basin, is consistent with the drying effect of the compensating subsidence induced by the enhanced precipitation in Northeast Brazil and in the extreme western portion of the Amazon basin where the moisture comes from the northeast (Venezuela and Colombia) from November to February (Ampuero et al. 2020). Thus, besides the ITCZ migration mechanism, there are different mechanisms responsible for subregional precipitation changes. Depending on the simulated strength of ITCZ over the Atlantic and the extent of the DY term over Northeast Brazil, our results suggest that the SAM is split in two antiphased subregions: one dominated by a dry continental regime in the central part of the domain (over Amazon) and one dominated by a wet Atlantic coastal regime (over Northeast Brazil) under the influence of the ITCZ dynamics and ventilation (advection of low moist static energy air from ocean regions into the summer continents; Su and Neelin 2005). Our findings would be

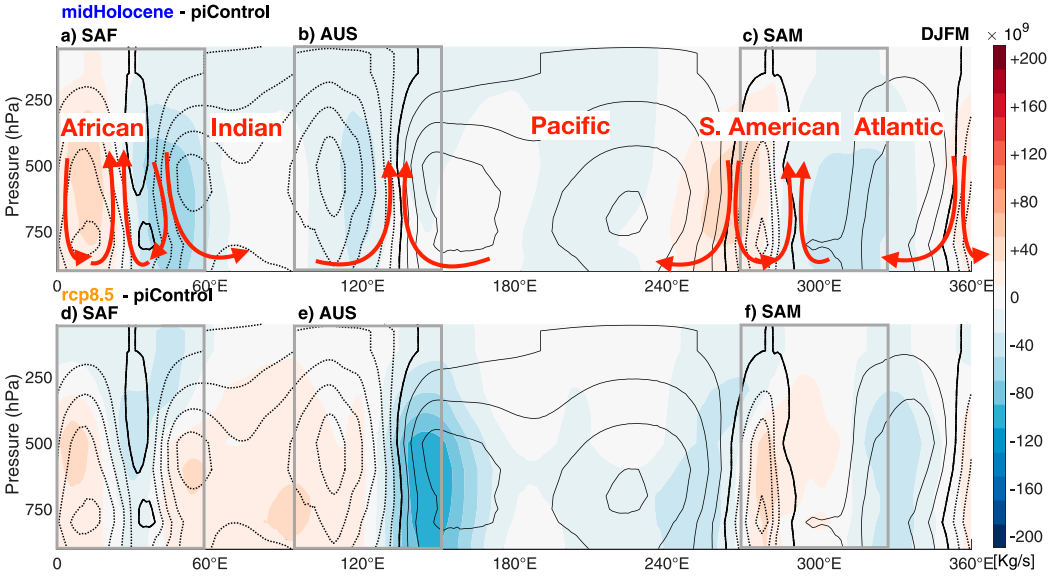

FIG. 6. Multimodel ensemble mean of DJFM Walker cell computed between 5°N and 5°S. Colors show the anomalous circulation in each experiment [(top) midHolocene; (bottom) RCP8.5] relative to piControl. Contours refer to piControl meridional mass streamfunction (contour step is 5×10^{10} kg s^{-1}). Solid (dotted) lines indicate positive (negative) values of the streamfunction for clockwise (counterclockwise) circulation. Arrows in the sketch indicates updrafts and downdrafts.

consistent with a possible extension of the mid-Holocene wet regime from Northeast Brazil coastal areas to the eastern Amazon catchment (Smith and Mayle 2018) and would reconcile the interpretation of Paraíso Cave speleothems showing a wettening tendency during the mid-Holocene (Wang et al. 2017).

b. SAF

Processes controlling the hydrological balance in South Africa on orbital to multidecadal time scales remain poorly understood because proxy records documenting its variability at high resolution are scarce. SAF is generally dominated by ITCZ shift across the equator, and by SST variations of adjacent oceans (Castañeda et al. 2009; Marchant et al. 2007; Acosta Navarro et al. 2017; Schefuß et al. 2005; Simon et al. 2015; Tierney et al. 2008).

An evaluation of six GCMs over East Africa reveals no clear multimodel trend in mean annual rainfall by 2080 (Conway et al. 2007), but hints to an increased precipitation. The changes are consistent with a differential warming of Indian Ocean SST, resulting in a zonal dipolelike state at the end of the twenty-first century (Stocker et al. 2014). This leads to a weakening of the descending branch of the East African Walker cell and an enhancement of low-level moisture flux convergence over East Africa (Vecchi and Soden 2007; Shongwe et al. 2011). In an assessment of 19 CMIP3 models run under A1B emissions, Giannini et al. (2008) note a tendency toward a persistent El Niño–like pattern in the equatorial Pacific along with a decreased rainfall over South Africa. However, the CMIP5 models projections of the twenty-first century show unaltered precipitation, without any clear response of the southeast African monsoon.

Our models subset shows expansion and strengthening of SAF in RCP8.5 ensemble mean relative to piControl (+2.8% and +3.8%, respectively; Table 1), with a positive $P - E$ balance in the continental area of rift lakes, from Ethiopian Highlands toward the south until Katanga Plateau (Fig. 2). This expansion is seen in all models (Table A1). However, only half of the models show increased precipitation (Table A1). The positive $P - E$ balance is due mainly to increased precipitation (Fig. 2e), but little to evaporation over the Ethiopian Highlands and African Horn (Fig. 2f). The increased rainfall in the Congo basin and Katanga Plateau region is attributed to TH changes (Fig. 4) because of increased deep convection associated with the stronger ascending branch of local Hadley circulation (Fig. 5). In contrast, the weakening and westward shift of the Atlantic and African Walker circulations (Fig. 6) result in reduced continental precipitation and in the DY weakening. Increased surface cyclonic circulation over the South Atlantic seems to reinforce the moisture transport toward western Africa coastal areas where the Res term is large (see TE and S terms in Figs. B1 and B2). Therefore, the cancellation between the TH and DY terms and the positive Res term (Fig. 4b) do not enable us to attribute such P changes to either TH or Res in the SAF domain, although P pattern resembles TH (Fig. 3).

In the midHolocene ensemble mean, the SAF monsoon contracts and precipitation decreases (−3.6% and −7.4% relative to piControl, Table 1). The monsoon contraction is seen in 6 out of 9 models while the precipitation decrease is seen in all 9 models (Table A1). The SAF response is also robust among models (Figs. A2, A3) with decreased precipitation due to DY weakening (Fig. 3), similar to other SH monsoon systems (Fig. 4a). The DY weakening over land results from a slowdown of local Hadley circulation (Fig. 5) and a clear increased moisture transport toward the Indian Ocean (Fig. 3) associated with the strengthening and westward shift of the Indian Walker circulation (Fig. 6), resulting from an asymmetric NEI anomaly between Atlantic and Indian Ocean (Fig. 1). Our results agree with Chevalier et al. (2017) on weaker SAF than present day and on the dynamic mechanisms as the leading factor explaining mid-Holocene precipitation anomalies.

c. AUS

Complex interaction between land and ocean characterizes the Maritime Continent region located between Asia and Australia. It provides a land bridge along which maximum convection migrates from the Asian summer monsoon (JJA) to the Australian monsoon (DJF) and vice versa. Northwest Australian summer rainfall has increased during recent decades by more than 50% (Dey et al. 2019), whereas northeast Australian summer rainfall has decreased markedly since around 1980 (Li et al. 2012). Models in general show skill in representing the spatial characteristics of AUS summer precipitation (CMIP3: Moise et al. 2012 and CMIP5: Brown et al. 2016). Based on an assessment of 33 CMIP5 models, AUS shows a wettening tendency more plausible than a drying by the end of the twenty-first century under RCP8.5. When a larger area is considered including the Maritime Continent region, as in this study, then a clearer signal of increased rainfall in future projections is found (e.g., Moise et al. 2012; Christensen et al. 2013).

Our models' subset supports the more plausible projected increase and expansion of the AUS ensemble mean under RCP8.5 (+8.2% relative to piControl, Table 1), in particular in its western region. The increased precipitation is shown in 6 out of 9 models, and the expansion by 100% of our model subset (Table A1). However, the evaporation in the surrounding ocean area

contributes to the overall $P - E$ budget. In this respect, the AUS changes are more driven by land–ocean NEI contrast (Fig. 1) than other SH monsoons. The increased wettening tendency over land appears to be related to the sign of surface fluxes (Figs. 1h,i) and hence to local ocean mean state. In fact, in RCP8.5, the moisture is advected to the Australian continent from surrounding oceans through an anomalous cyclonic near-surface atmospheric circulation, whose center of action is located over the arid central Australia, resembling a reinforced heat low (analogous with the Saharan heat low). In the current climate, the moisture convergence into the heat low has been found to be important for regulating convection over northern Australia (Arnup and Reeder 2007; Berry et al. 2011; Lavender 2017), and it also influences the monsoon by transporting moist air inland, intensifying the monsoon circulation itself (e.g., Hung and Yanai 2004). Under future warming, in our models subset, the DY and therefore the local circulation advects moisture from the Indian Ocean to western coasts and from the Pacific Ocean to eastern coasts, both areas not included in the considered land-only monsoon domain (see orange line in Fig. 1). On the other hand, the northern coast is much more affected by the TH component, related to increased moisture in the Maritime Continent. Moreover, the Res term is large along the coasts where the TE contribution is particularly important (Figs. B1, B2). Therefore, in the AUS monsoon region (and the SH monsoon), the wettening tendency under RCP8.5 forcing is attributed to the increased TH component (with low intermodel spread, Fig. A3), and its compensation with the DY depends on local circulation pattern (e.g., the strengthening and the position of the anomalous near-surface heat low), the magnitude and position of which is strongly model dependent in the warm pool region (Fig. A3). Here, local Hadley and Walker cells (Figs. 4, 6) are much weaker than in other domains consistent with the strong DY weakening in the Maritime Continent (Fig. 3). In addition, the strengthening of the ascending branch of the local Hadley circulation indicates a deeper convection, and potentially a more stable troposphere as suggested by Chou and Chen (2010).

In the midHolocene ensemble mean, the AUS shows strong monsoon contraction and precipitation decrease (−13.8% and −10.5% relative to piControl, Table 1). The change is robust among our model subset (Table A1). The midHolocene AUS conditions are driven by the negative NEI change and primarily by the DY weakening (Fig. 3). The DY weakening is associated with reversed near-surface atmospheric circulation (see anomalous vectors in Fig. 3): the reinforced anticyclonic and stable conditions prevent the inland advection of moisture from adjacent oceans. This is consistent with strengthening and contraction of the Hadley Cell (Fig. 5). Moisture is transported away from continents, converging over tropical oceans (Fig. 3) mainly due to zonal shift of Walker circulation center of action: the Indian Walker is stronger and narrower than piControl, with the main updraft in the AUS domain shifted westward around 110°E longitude (Fig. 6). Our model results agree with proxy records that indicate reduced AUS monsoon precipitation in the mid-Holocene (Mohtadi et al. 2011; McGowan et al. 2012; Denniston et al. 2013). The disagreement with other records showing increased mid-Holocene AUS monsoon precipitation (Johnson et al. 1999; Magee et al. 2004; Shulmeister 1999; Rowe 2007) may be due to differences in regional responses across northern Australia or the timing of precipitation changes and will require further studies to reconcile.

5. Conclusions

Atmospheric hydrological balance changes in SH monsoons are investigated in an ensemble of climate model simulations for midHolocene and greenhouse gas–induced global warming scenario RCP8.5 with reference to piControl in context of an energetic framework. Given that these two experiments are driven by different forcing (orbital vs greenhouse gases), their atmospheric net energy input (NEI) anomaly is very different from each other and relative to piControl. This difference helps to understand the link between precipitation and NEI changes. In a steady state, the vertically integrated MSE divergence, used as a proxy for tropical precipitation, is balanced by the atmospheric NEI. We make use of the energetic framework to find contrasting behaviors among SH monsoons in past and future climates. Currently, SH monsoons are less investigated because of the scarce data reconstructions in the mid-Holocene and less understood because of the large intermodel spread in RCP8.5 simulations.

To better address past and future changes in SH monsoons, the moisture budget has been decomposed into two main components: thermodynamic (TH) and dynamic (DY). The change in TH describes the relative change in specific humidity between the target climate (midHolocene or RCP8.5) and the reference climate (piControl), assuming no changes in the moisture contribution given by the atmospheric circulation (fixed to piControl). The change in DY describes the relative moisture contribution because of atmospheric mean flow changes (i.e., Walker and Hadley circulations in the tropics) between the target climate and the reference climate, assuming no changes in the specific humidity content. Main findings are summarized below.

TABLE A1. Values of anomalous monsoon extent and strength in the midHolocene and RCP8.5 relative to piControl for each model and for each monsoon domain. Maxima and minima are in bold.

	δExtent (10^6 km^2)								δStrength (mm day^{-1})							
	MidHolocene				RCP8.5				MidHolocene				RCP8.5			
	SAM	SAF	AUS	SH	SAM	SAF	AUS	SH	SAM	SAF	AUS	SH	SAM	SAF	AUS	SH
BCC_CSM1.1	**−0.69**	−0.48	−0.45	**−1.61**	−0.05	0.33	0.15	0.43	−0.47	−0.53	−0.43	−0.48	0.28	0.33	0.38	0.32
CCSM4	−0.18	−0.35	−0.56	−1.08	−0.03	0.14	0.63	0.74	**−0.31**	−0.46	−0.55	−0.41	0.41	0.54	1.14	0.62
CSIRO Mk3.6-0	−0.05	0.02	−0.46	**−0.49**	**−0.29**	**0.02**	**−0.86**	**−1.13**	−0.54	−0.60	−0.35	−0.52	0.40	**−0.47**	**−0.99**	**−0.15**
CNRM-CM5	**0.03**	**−0.55**	−0.55	−1.07	0.13	0.23	0.89	1.25	−0.42	−0.32	−0.29	**−0.36**	0.39	0.32	0.59	0.41
FGOALS-g2	−0.18	−0.55	**−0.26**	−0.99	0.43	0.04	0.10	0.57	−0.47	−0.52	**0.07**	−0.42	0.74	−0.05	1.28	0.54
HadGEM2-ES	−0.29	0.01	−0.57	−0.86	−0.04	0.25	0.40	0.61	−0.57	**−0.09**	**−0.79**	−0.42	0.04	−0.23	0.34	−0.01
IPSL-CM5A-LR	−0.22	−0.43	**−0.68**	−1.33	0.10	**0.40**	−0.04	0.48	−0.51	−0.56	−0.73	−0.54	1.08	**1.37**	**2.31**	**1.30**
MIROC-ESM	−0.15	**0.07**	**−0.68**	−0.76	0.68	0.13	**1.14**	**1.93**	−0.55	**−0.78**	−0.68	**−0.66**	**−0.15**	0.05	−0.18	−0.09
MRI-CGCM3	−0.26	−0.21	−0.65	−1.11	**1.11**	**0.40**	0.01	1.52	**−0.88**	−0.20	−0.65	−0.60	**1.08**	−0.13	0.92	0.6
Ensemble mean	−0.22	−0.27	−0.54	−1.03	0.23	0.22	0.27	0.71	−0.52	−0.45	−0.49	−0.49	0.47	0.19	0.64	0.39

Based on the PMIP3–CMIP5 multimodel mean (9 models), we find a weakening and contraction of the SH monsoon in the midHolocene and a strengthening and expansion in RCP8.5, consistently with results based on the newest generation of PMIP4–CMIP6 (Brierley et al. 2020; Fiedler et al. 2020). The change is less than 10%, which is smaller than the intermodel range in some areas. However, there is a general model consensus on the direction of change in all regional SH monsoons suggesting a reasonable agreement on the large-scale response.

The contraction and weakening of SH monsoons under midHolocene forcing are mainly dominated by DY decrease. The very small TH weakening results from the very small moisture and temperature change (−0.3 K, Fig. 1e) and/or the hemispherically reduced insolation and NEI.

In contrast, the expansion and intensification of SH monsoons under RCP8.5 is dominated by the strong positive TH component relative to piControl, especially over land and warm pool region. TH increases because moisture follows the greenhouse gas–induced warming (292.1 and 288.7 K in RCP8.5 and piControl, respectively, Fig. 1j).

Change in NEI explains most of the change in monsoonal precipitation under midHolocene forcing. All three regional and SH monsoons exhibit DY and NEI weakening and reduced precipitation. Furthermore, land–ocean precipitation contrast is associated with weakening of local atmospheric circulation land and strengthening over ocean. In particular, mean flow intensification over Atlantic and Indian Oceans is mainly due to the shift and strengthening of local Walker circulation over those oceans.

Under RCP8.5 forcing, the changes are less clear. While increased monsoonal precipitation is consistent with positive change in NEI, the DY term is negative and the TH term is largely positive. Given the Hadley and Walker circulations are weakening and there is a negligible shift of their ascending branches, the excess of NEI cannot be exported away by the circulation. Therefore, the anomalous NEI likely cannot be exported away by the circulation without a change in the GMS (Neelin and Held 1987). However, the relative role of change in stratification versus circulation strength for explaining NEI changes under global warming deserves further investigation, which is beyond the scope of current work.

Acknowledgments. R. D. was supported by the JPI–Belmont Forum's project PaCMEDy: Paleo Constraint on Monsoon Evolution and Dynamics. P. L. S. D. acknowledges the FAPESP support under the PaCMEDy program (Grant 2015/50686-1). R. D. conceived and designed the study, analyzed the simulations, and prepared the figures and the manuscript. All authors contributed to the interpretation of results and to the writing of the manuscript. We thank David Ferreira and Juergen Bader and the three anonymous reviewers for their comments and suggestions on the draft. We acknowledge the World Climate Research Programmes Working Group on Coupled Modelling, which is responsible for CMIP. PMIP3 and CMIP5 data are available at https://esgf-data.dkrz.de/search/cmip5-dkrz/. Scripts used in the analysis and other supporting information useful to reproduce the author's work are archived by the Max Planck Institute for Meteorology and can be obtained contacting publications@mpimet.mpg.de.

APPENDIX A

Intermodel Spread on Precipitation Minus Evaporation

Table A1 shows anomalous monsoon extent and strength in the midHolocene and RCP8.5 relative to piControl for each model and monsoon domain.

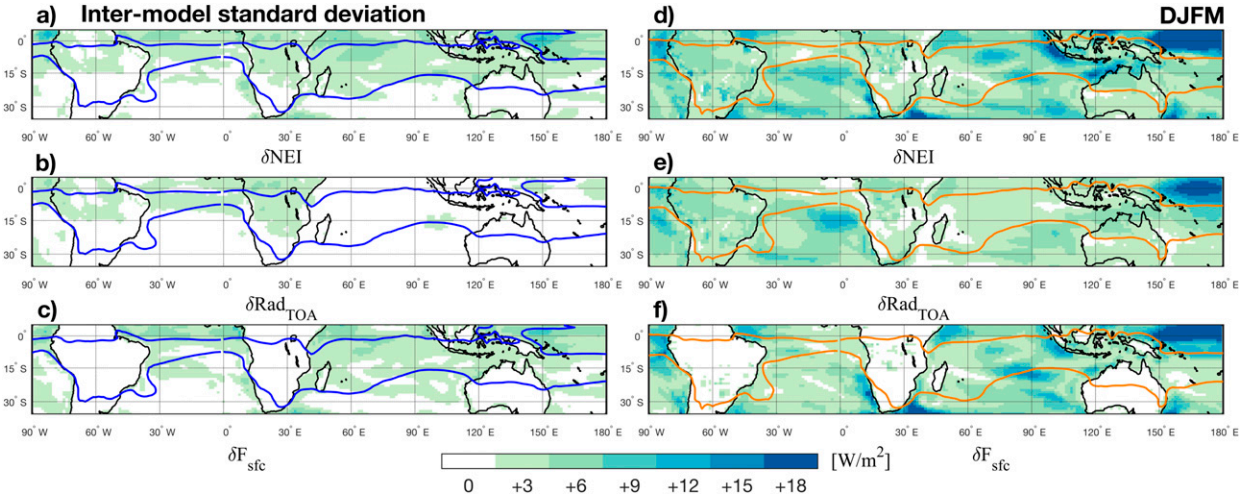

FIG. A1. Standard deviation of NEI, Rad_{toa}, and F_{sfc} for (a)–(c) midHolocene and (d)–(f) RCP8.5 among ensemble members in DJFM (shading). Orange and blue bold lines show areas within which the annual precipitation range (DJFM minus JJAS) exceeds 2 mm day^{-1} for RCP8.5 and midHolocene, respectively.

Figures A1, A2, A3 show intermodel spread for NEI, with its components, hydrological cycle, and moisture budget components, respectively.

Figure A1 shows that the standard deviation of NEI is strongest over the ocean, and stronger in RCP8.5, resulting from the combined effect of radiative and surface fluxes. Over land, the spread is small and arises from top-of-atmosphere radiation fluxes.

Figure A2 shows that most of the intermodel standard deviation of precipitation minus evaporation ($P - E$) in DJFM for all monsoon regions arises from precipitation. The largest model spread (i.e., strongest standard deviation) is located in the Maritime Continent and in Northeast Brazil, and it is much more pronounced in RCP8.5 than in the midHolocene.

Figure A3 shows that while the standard deviation is very small in the midHolocene, it becomes non-negligible in RCP8.5. The spread is particularly large in the Maritime Continent in the DY and Res terms, in the Pacific coastal South America in the TH and Res terms,

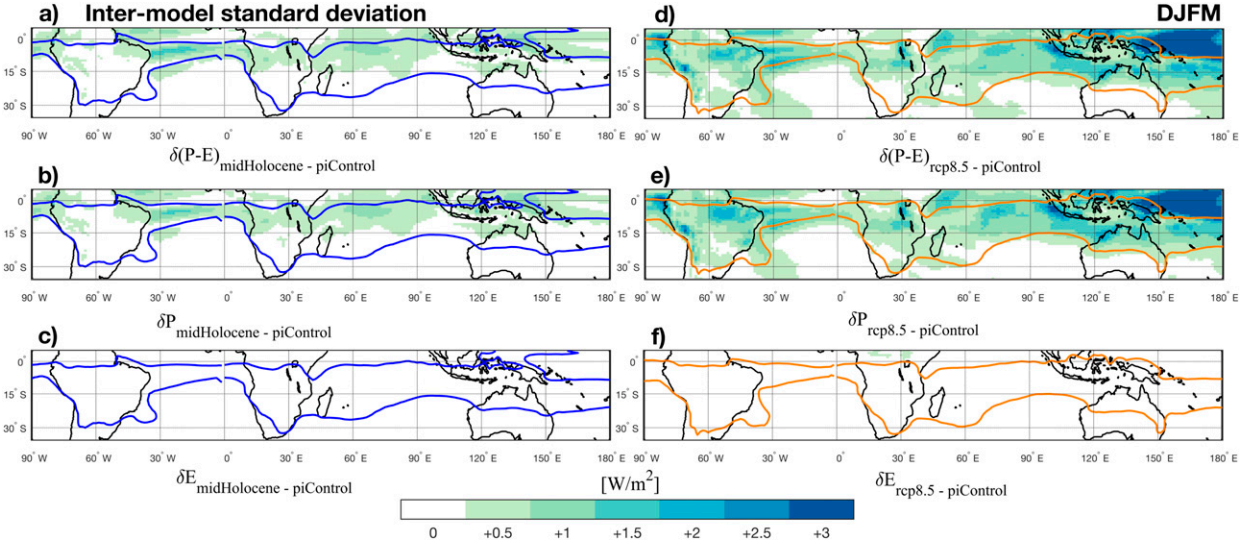

FIG. A2. Standard deviation among ensemble members for changes in $P - E$, precipitation, and evaporation for (a)–(c) midHolocene and (d)–(f) RCP8.5 in DJFM (shading). Orange and blue bold lines show areas within which the annual precipitation range (DJFM minus JJAS) exceeds 2 mm day^{-1} for RCP8.5 and midHolocene, respectively.

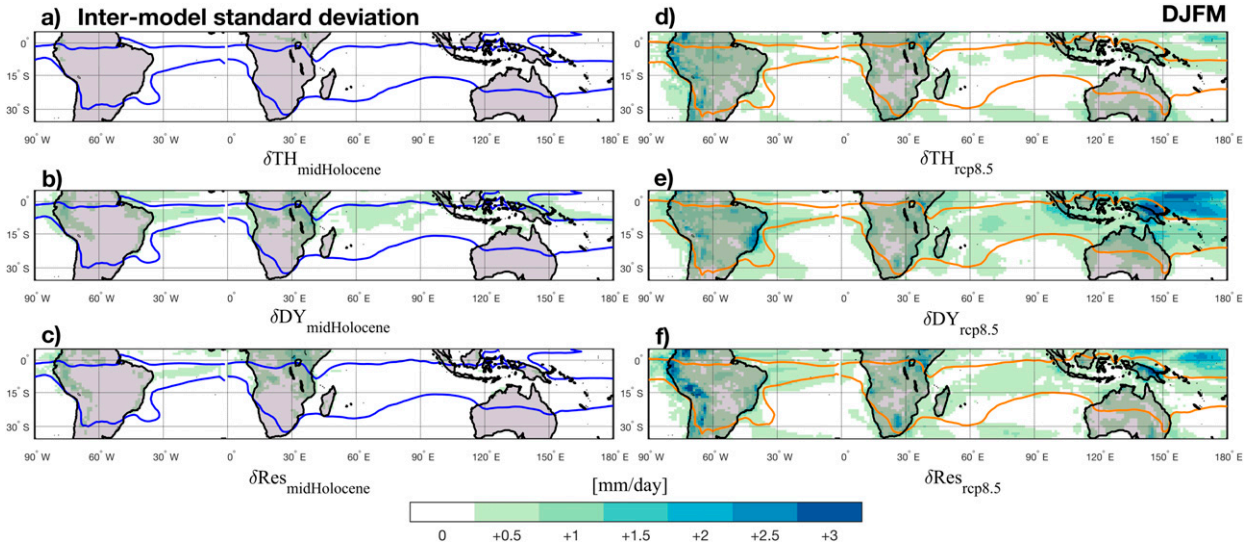

FIG. A3. Standard deviation computed for TH and DY components of the moisture budget for (a),(b) midHolocene and (d),(e) RCP8.5 among ensemble members in DJFM (shading). (c),(f) The standard deviation of the Res. Orange and blue bold lines show areas within which the annual precipitation range (DJFM minus JJAS) exceeds 2 mm day^{-1} for RCP8.5 and midHolocene, respectively.

in Atlantic coastal South America in the DY term, and in southeast Africa in the Res term.

APPENDIX B

Moisture Budget Decomposition: Transient Eddy and Surface Terms

Here, we provide additional information on the moisture budget method to support our results. The moisture budget decomposition used to interpret the different monsoon response in the two experiments follows these equations:

$$\rho_w g(\overline{P} - \overline{E}) = -\int_{p_t}^{p_s} (\overline{\mathbf{u}} \cdot \nabla \overline{q} + \overline{q} \nabla \cdot \overline{\mathbf{u}})\, dp - \text{Res}, \qquad \text{(B1)}$$

where Res is the residual composed as

$$\text{Res} = \int_{p_t}^{p_s} \nabla \cdot (\overline{\mathbf{u}'q'})\, dp + S. \qquad \text{(B2)}$$

The overbars indicate monthly means and primes indicate departure from the monthly mean, p is pressure, q is specific

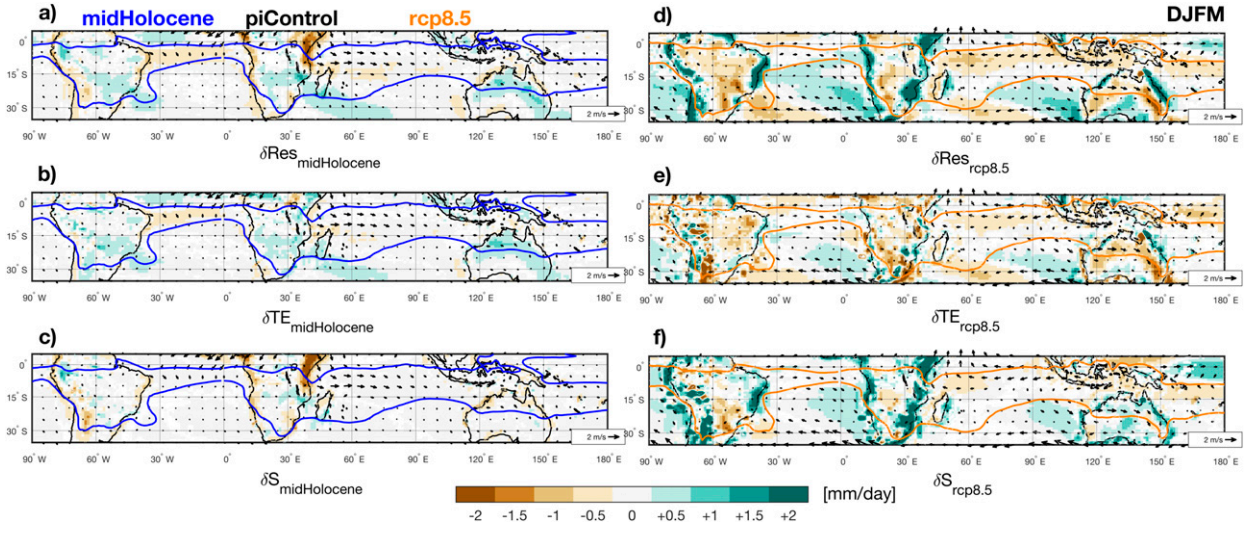

FIG. B1. (a),(d) Res is decomposed in changes in TE and S terms of the moisture budget for (b),(c) midHolocene and (e),(f) RCP8.5 in DJFM ensemble means (shading). Vectors are 925-hPa wind anomalies for midHolocene and RCP8.5 relative to piControl.

humidity, $\overline{\mathbf{u}}$ is the horizontal vector wind, ρ_w is the water density, and S is surface quantity. All integrals are computed between the top and surface (respectively p_t and p_s) pressure levels on which every model has been vertically interpolated (1000, 925, 850, 700, 600, 500, 400, 300, 250, 200, 150, 100, 70, 50, 30, 20, and 10 hPa). Following Trenberth and Guillemot (1995), Seager et al. (2010), D'Agostino et al. (2019), and D'Agostino and Lionello (2020), the anomalous moisture budget can be decomposed as

$$\rho_w g\delta(\overline{P}-\overline{E}) = -\int_{p_t}^{p_s}(\overline{\mathbf{u}}_{\text{piControl}}\cdot\nabla\delta\overline{q}+\delta\overline{q}\nabla\cdot\overline{\mathbf{u}}_{\text{piControl}})\,dp + -\int_{p_t}^{p_s}(\delta\overline{\mathbf{u}}\cdot\nabla\overline{q}_{\text{piControl}}+\overline{q}_{\text{piControl}}\nabla\cdot\delta\overline{\mathbf{u}})\,dp + -\int_{p_t}^{p_s}\nabla\cdot\delta(\overline{\mathbf{u}'q'})\,dp-\delta S, \tag{B3}$$

where every δ describes the difference between each experiment (midHolocene or RCP8.5) and the reference climate (piControl):

$$\delta(\cdot)=(\cdot)_{\text{midHolocene\_or\_rcp8.5}}-(\cdot)_{\text{piControl}}, \tag{B4}$$

and we have neglected quadratic terms. The lowest level has been replaced by surface pressure. The first integral on the right-hand side of Eq. (B3) describes the change in specific humidity (decomposed into advective and divergent terms), while the second integral describes the moisture flux convergence by the mean flow, also decomposed into its advective and divergent terms. The third term describes contribution from the TE, and the last term involves surface quantities S. In Eq. (B3), the terms involving $\delta\overline{q}$ but no changes in $\overline{\mathbf{u}}$ are referred to as the TH to $\delta(\overline{P}-\overline{E})$ and the terms involving $\delta\overline{\mathbf{u}}$ but no changes in $\overline{q}$ as DY.

Because only data at monthly resolution are available for all models, the δTE component cannot be computed explicitly, but is estimated as a residual:

$$\delta\text{TE}=\rho_w g\delta(\overline{P}-\overline{E})-\delta\text{TH}-\delta\text{DY}-\delta S, \tag{B5}$$

where specifically,

$$\delta\text{TH}=-\frac{1}{\rho_w g}\int_{p_t}^{p_s}(\overline{\mathbf{u}}_{\text{piControl}}\cdot\nabla\delta\overline{q}+\delta\overline{q}\nabla\cdot\overline{\mathbf{u}}_{\text{piControl}})\,dp, \tag{B6}$$

$$\delta\text{DY}=-\frac{1}{\rho_w g}\int_{p_t}^{p_s}(\delta\overline{\mathbf{u}}\cdot\nabla\overline{q}_{\text{piControl}}+\overline{q}_{\text{piControl}}\nabla\cdot\delta\overline{\mathbf{u}})\,dp, \quad \text{and} \tag{B7}$$

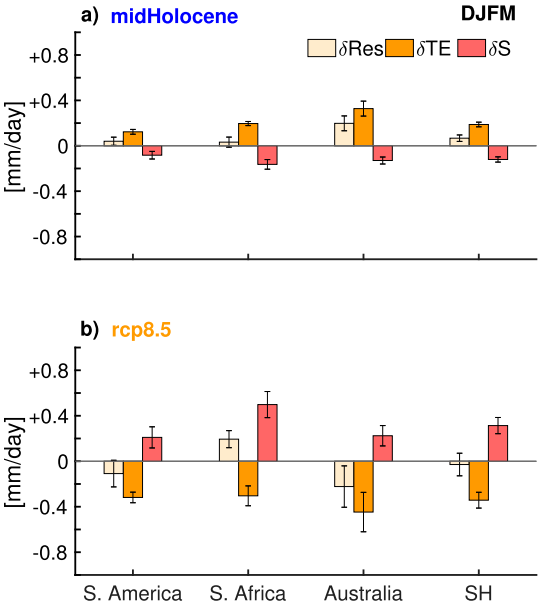

FIG. B2. Regionally averaged Res, TE, and S terms of the moisture budget for (a) midHolocene and (b) RCP8.5 (black axis). Bar ranges indicate the standard error for each contribution computed among the ensemble members.

$$\delta S=-\frac{1}{\rho_w g}\nabla\cdot\delta\int_{p_t}^{p_s}(\overline{\mathbf{u}}\cdot\overline{q})\,dp-\delta\text{TH}-\delta\text{DY}. \tag{B8}$$

In this case, δTE also includes the nonlinear terms, which are much smaller.

Figure B1 shows the δRes, δTE, and δS for SH, and Fig. B2 shows their regional averages for every monsoon region.

APPENDIX C

Local Meridional and Zonal Mass Streamfunction

Following the approach of Schwendike et al. (2015) and Nguyen et al. (2018), the atmospheric vertical motion in pressure coordinates can be decomposed into zonal and meridional overturning. In this study, we computed a local meridional and zonal mass streamfunction to describe Hadley and Walker circulation changes, respectively. First, horizontal winds are decomposed into rotational and divergent components in spherical coordinates (only the latter contributes to the vertical motion). The divergent component of the meridional flow is related to the Hadley circulation and the divergent component of the zonal flow to the Walker circulation. Mass continuity for the divergent circulation is satisfied independently in the zonal and meridional

directions because the two circulations are in orthogonal planes. Meridional and zonal overturning circulation can be represented by a streamfunction, derived from the divergent meridional v_d and zonal u_d winds, as

$$\psi_y(y, p) = -\frac{2\pi R \cos y}{g}\int_{p_t}^{p_s}[v_d(y, p)]\,dp, \quad \text{and} \qquad \text{(C1)}$$

$$\psi_x(x, p) = -\frac{2\pi R}{g}\int_{p_t}^{p_s}[u_d(x, p)]\,dp. \qquad \text{(C2)}$$

Brackets in this case refer to a zonal average over a specified limited (or hemispheric) domain. Here, R is Earth's radius, g is the gravity acceleration, p_t is pressure at the top of troposphere (here we used 100 hPa), and p_s is the surface pressure field.

This method ensures the decomposition of the divergent motion into two unique orthogonal overturning circulations that are the sum of the total divergent flow.

Figure 5 shows the Walker circulation: the vertically integrated zonal divergent winds have been area averaged along the equator between 5°N and 5°S, where the overturning presents the mean ascents (Webster and Yang 1992; Bell and Halpert 1998; Yu and Zwiers 2010).

REFERENCES

Acosta Navarro, J. C., and Coauthors, 2017: Future response of temperature and precipitation to reduced aerosol emissions as compared with increased greenhouse gas concentrations. *J. Climate*, **30**, 939–954, https://doi.org/10.1175/JCLI-D-16-0466.1.

Ampuero, A., and Coauthors, 2020: The forest effects on the isotopic composition of rainfall in the northwestern Amazon basin. *J. Geophys. Res. Atmos.*, **125**, e2019JD031445, https://doi.org/10.1029/2019jd031445.

Arnup, S. J., and M. J. Reeder, 2007: The diurnal and seasonal variation of the northern Australian dryline. *Mon. Wea. Rev.*, **135**, 2995–3008, https://doi.org/10.1175/MWR3455.1.

Bell, G. D., and M. S. Halpert, 1998: Climate assessment for 1997. *Bull. Amer. Meteor. Soc.*, **79** (5s), S1–S50, https://doi.org/10.1175/1520-0477-79.5s.S1.

Berry, G., M. J. Reeder, and C. Jakob, 2011: Physical mechanisms regulating summertime rainfall over northwestern Australia. *J. Climate*, **24**, 3705–3717, https://doi.org/10.1175/2011JCLI3943.1.

Biasutti, M., 2013: Forced Sahel rainfall trends in the CMIP5 archive. *J. Geophys. Res. Atmos.*, **118**, 1613–1623, https://doi.org/10.1002/JGRD.50206.

——, and Coauthors, 2018: Global energetics and local physics as drivers of past, present and future monsoons. *Nat. Geosci.*, **11**, 392–400, https://doi.org/10.1038/s41561-018-0137-1.

Bischoff, T., T. Schneider, and A. N. Meckler, 2017: A conceptual model for the response of tropical rainfall to orbital variations. *J. Climate*, **30**, 8375–8391, https://doi.org/10.1175/JCLI-D-16-0691.1.

Boisier, J. P., P. Ciais, A. Ducharne, and M. Guimberteau, 2015: Projected strengthening of Amazonian dry season by constrained climate model simulations. *Nat. Climate Change*, **5**, 656–660, https://doi.org/10.1038/nclimate2658.

Boos, W. R., and R. L. Korty, 2016: Regional energy budget control of the intertropical convergence zone and application to mid-Holocene rainfall. *Nat. Geosci.*, **9**, 892–897, https://doi.org/10.1038/ngeo2833.

Bordoni, S., and T. Schneider, 2008: Monsoons as eddy-mediated regime transitions of the tropical overturning circulation. *Nat. Geosci.*, **1**, 515–519, https://doi.org/10.1038/ngeo248.

Braconnot, P., O. Marti, S. Joussaume, and Y. Leclainche, 2000: Ocean feedback in response to 6 kyr BP insolation. *J. Climate*, **13**, 1537–1553, https://doi.org/10.1175/1520-0442(2000)013<1537:OFIRTK>2.0.CO;2.

——, and Coauthors, 2007: Results of PMIP2 coupled simulations of the mid-Holocene and last glacial maximum—Part 1: Experiments and large-scale features. *Climate Past*, **3**, 261–277, https://doi.org/10.5194/cp-3-261-2007.

Brierley, C., and Coauthors, 2020: Large-scale features and evaluation of the PMIP4-CMIP6 *midHolocene* simulations. *Climate Past Discuss.*, https://doi.org/10.5194/cp-2019-168, in press.

Brown, J. R., A. F. Moise, R. Colman, and H. Zhang, 2016: Will a warmer world mean a wetter or drier Australian monsoon? *J. Climate*, **29**, 4577–4596, https://doi.org/10.1175/JCLI-D-15-0695.1.

Castañeda, I. S., J. P. Werne, and T. C. Johnsona, 2009: Influence of climate change on algal community structure and primary productivity of Lake Malawi (East Africa) from the last glacial maximum to present. *Limnol. Oceanogr.*, **54**, 2431–2447, https://doi.org/10.4319/lo.2009.54.6_part_2.2431.

Chadwick, R., I. Boutle, and G. Martin, 2013: Spatial patterns of precipitation change in CMIP5: Why the rich do not get richer in the tropics. *J. Climate*, **26**, 3803–3822, https://doi.org/10.1175/JCLI-D-12-00543.1.

Chevalier, M., S. Brewer, and B. M. Chase, 2017: Qualitative assessment of PMIP3 rainfall simulations across the eastern African monsoon domains during the mid-Holocene and the Last Glacial Maximum. *Quat. Sci. Rev.*, **156**, 107–120, https://doi.org/10.1016/j.quascirev.2016.11.028.

Chou, C., and C.-A. Chen, 2010: Depth of convection and the weakening of tropical circulation in global warming. *J. Climate*, **23**, 3019–3030, https://doi.org/10.1175/2010JCLI3383.1.

——, J. Neelin, and H. Su, 2001: Ocean-atmosphere-land feedbacks in an idealized monsoon. *Quart. J. Roy. Meteor. Soc.*, **127**, 1869–1891, https://doi.org/10.1002/qj.49712757602.

Christensen, J. H., and Coauthors, 2013: Climate phenomena and their relevance for future regional climate change. *Climate Change 2013: The Physical Science Basis*, T. F. Stocker et al., Eds., Cambridge University Press, 1217–1308.

Conway, D., C. Hanson, R. Doherty, and A. Persechino, 2007: Gcm simulations of the Indian Ocean dipole influence on East African rainfall: Present and future. *Geophys. Res. Lett.*, **34**, L03705, https://doi.org/10.1029/2006GL027597.

Cook, B., and R. Seager, 2013: The response of the North American monsoon to increased greenhouse gas forcing. *J. Geophys. Res. Atmos.*, **118**, 1690–1699, https://doi.org/10.1002/JGRD.50111.

Cruz, F. W., and Coauthors, 2009: Orbitally driven east–west antiphasing of South American precipitation. *Nat. Geosci.*, **2**, 210–214, https://doi.org/10.1038/ngeo444.

D'Agostino, R., and P. Lionello, 2020: The atmospheric moisture budget in the Mediterranean: Mechanisms for seasonal changes in the Last Glacial Maximum and future warming scenario. *Quat. Sci. Rev.*, **241**, 106392, https://doi.org/10.1016/j.quascirev.2020.106392.

——, J. Bader, S. Bordoni, D. Ferreira, and J. Jungclaus, 2019: Northern Hemisphere monsoon response to mid-Holocene

orbital forcing and greenhouse gas-induced global warming. *Geophys. Res. Lett.*, **46**, 1591–1601, https://doi.org/10.1029/2018GL081589.

da Silva, A. E., and L. M. V. de Carvalho, 2007: Large-Scale Index for South America Monsoon (LISAM). *Atmos. Sci. Lett.*, **8**, 51–57, https://doi.org/10.1002/asl.150.

Denniston, R. F., and Coauthors, 2013: A stalagmite record of Holocene Indonesian–Australian summer monsoon variability from the Australian tropics. *Quat. Sci. Rev.*, **78**, 155–168, https://doi.org/10.1016/j.quascirev.2013.08.004.

Dey, R., S. C. Lewis, and N. J. Abram, 2019: Investigating observed northwest Australian rainfall trends in Coupled Model Intercomparison project phase 5 detection and attribution experiments. *Int. J. Climatol.*, **39**, 112–127, https://doi.org/10.1002/joc.5788.

Donohoe, A., 2016: Energy and precipitation. *Nat. Geosci.*, **9**, 861–862, https://doi.org/10.1038/ngeo2846.

Endo, H., and A. Kitoh, 2014: Thermodynamic and dynamic effects on regional monsoon rainfall changes in a warmer climate. *Geophys. Res. Lett.*, **41**, 1704–1711, https://doi.org/10.1002/2013GL059158.

Fiedler, S., and Coauthors, 2020: Simulated tropical precipitation assessed across three major phases of the Coupled Model Intercomparison Project (CMIP). *Mon. Wea. Rev.*, **148**, 3653–3680, https://doi.org/10.1175/MWR-D-19-0404.1.

Fleitmann, D., S. J. Burns, M. Mudelsee, U. Neff, J. Kramers, A. Mangini, and A. Matter, 2003: Holocene forcing of the Indian monsoon recorded in a stalagmite from southern Oman. *Science*, **300**, 1737–1739, https://doi.org/10.1126/science.1083130.

Gaetani, M., C. Flamant, S. Bastin, S. Janicot, C. Lavaysse, F. Hourdin, P. Braconnot, and S. Bony, 2017: West African monsoon dynamics and precipitation: The competition between global SST warming and CO_2 increase in CMIP5 idealized simulations. *Climate Dyn.*, **48**, 1353–1373, https://doi.org/10.1007/s00382-016-3146-z.

Giannini, A., M. Biasutti, I. M. Held, and A. H. Sobel, 2008: A global perspective on African climate. *Climatic Change*, **90**, 359–383, https://doi.org/10.1007/s10584-008-9396-y.

Haug, G. H., K. A. Hughen, D. M. Sigman, L. C. Peterson, and U. Röhl, 2001: Southward migration of the intertropical convergence zone through the Holocene. *Science*, **293**, 1304–1308, https://doi.org/10.1126/science.1059725.

Heaviside, C., and A. Czaja, 2013: Deconstructing the Hadley cell heat transport. *Quart. J. Roy. Meteor. Soc.*, **139**, 2181–2189, https://doi.org/10.1002/qj.2085.

Held, I. M., and B. J. Soden, 2006: Robust responses of the hydrological cycle to global warming. *J. Climate*, **19**, 5686–5699, https://doi.org/10.1175/JCLI3990.1.

Hély, C., and A.-M. Lézine, 2014: Holocene changes in African vegetation: Tradeoff between climate and water availability. *Climate Past*, **10**, 681–686, https://doi.org/10.5194/cp-10-681-2014.

Hsu, P., T. Li, J.-J. Luo, H. Murakami, A. Kitoh, and M. Zhao, 2012: Increase of global monsoon area and precipitation under global warming: A robust signal? *Geophys. Res. Lett.*, **39**, L06701, https://doi.org/10.1029/2012GL051037.

Hsu, Y.-H., C. Chou, and K.-Y. Wei, 2010: Land–ocean asymmetry of tropical precipitation changes in the mid-Holocene. *J. Climate*, **23**, 4133–4151, https://doi.org/10.1175/2010JCLI3392.1.

Hung, C.-W., and M. Yanai, 2004: Factors contributing to the onset of the Australian summer monsoon. *Quart. J. Roy. Meteor. Soc.*, **130**, 739–758, https://doi.org/10.1256/qj.02.191.

Johnson, B., G. H. Miller, M. L. Fogel, J. Magee, M. Gagan, and A. Chivas, 1999: 65,000 years of vegetation change in central Australia and the Australian summer monsoon. *Science*, **284**, 1150–1152, https://doi.org/10.1126/science.284.5417.1150.

Jones, C., and L. M. Carvalho, 2013: Climate change in the South American monsoon system: Present climate and CMIP5 projections. *J. Climate*, **26**, 6660–6678, https://doi.org/10.1175/JCLI-D-12-00412.1.

Jourdain, N. C., A. S. Gupta, A. S. Taschetto, C. C. Ummenhofer, A. F. Moise, and K. Ashok, 2013: The Indo-Australian monsoon and its relationship to ENSO and IOD in reanalysis data and the CMIP3/CMIP5 simulations. *Climate Dyn.*, **41**, 3073–3102, https://doi.org/10.1007/s00382-013-1676-1.

Kitoh, A., H. Endo, K. Krishna Kumar, I. F. Cavalcanti, P. Goswami, and T. Zhou, 2013: Monsoons in a changing world: A regional perspective in a global context. *J. Geophys. Res. Atmos.*, **118**, 3053–3065, https://doi.org/10.1002/JGRD.50258.

Kodama, Y., 1992: Large-scale common features of subtropical precipitation zones (the Baiu frontal zone, the SPCZ, and the SACZ). Part I: Characteristics of subtropical frontal zones. *J. Meteor. Soc. Japan*, **70**, 813–836, https://doi.org/10.2151/jmsj1965.70.4_813.

——, 1993: Large-scale common features of sub-tropical convergence zones (the Baiu frontal zone, the SPCZ, and the SACZ). Part II: Conditions of the circulations for generating the STCZS. *J. Meteor. Soc. Japan*, **71**, 581–610, https://doi.org/10.2151/jmsj1965.71.5_581.

Krause, C. E., and Coauthors, 2019: Spatio-temporal evolution of Australasian monsoon hydroclimate over the last 40,000 years. *Earth Planet. Sci. Lett.*, **513**, 103–112, https://doi.org/10.1016/j.epsl.2019.01.045.

Lavender, S. L., 2017: A climatology of Australian heat low events. *Int. J. Climatol.*, **37**, 534–539, https://doi.org/10.1002/joc.4692.

Lee, J.-Y., and B. Wang, 2014: Future change of global monsoon in the CMIP5. *Climate Dyn.*, **42**, 101–119, https://doi.org/10.1007/s00382-012-1564-0.

Lembo, V., D. Folini, M. Wild, and P. Lionello, 2019: Inter-hemispheric differences in energy budgets and cross-equatorial transport anomalies during the 20th century. *Climate Dyn.*, **53**, 115–135, https://doi.org/10.1007/s00382-018-4572-x.

Levermann, A., J. Schewe, V. Petoukhov, and H. Held, 2009: Basic mechanism for abrupt monsoon transitions. *Proc. Natl. Acad. Sci. USA*, **106**, 20 572–20 577, https://doi.org/10.1073/pnas.0901414106.

Lézine, A.-M., C. Hély, C. Grenier, P. Braconnot, and G. Krinner, 2011: Sahara and Sahel vulnerability to climate changes, lessons from Holocene hydrological data. *Quat. Sci. Rev.*, **30**, 3001–3012, https://doi.org/10.1016/j.quascirev.2011.07.006.

Li, J., J. Feng, and Y. Li, 2012: A possible cause of decreasing summer rainfall in northeast Australia. *Int. J. Climatol.*, **32**, 995–1005, https://doi.org/10.1002/joc.2328.

Liu, J., B. Wang, Q. Ding, X. Kuang, W. Soon, and E. Zorita, 2009: Centennial variations of the global monsoon precipitation in the last millennium: Results from ECHO-G model. *J. Climate*, **22**, 2356–2371, https://doi.org/10.1175/2008JCLI2353.1.

Liu, Z., and Z. Ding, 1998: Chinese loess and the paleomonsoon. *Annu. Rev. Earth Planet. Sci.*, **26**, 111–145, https://doi.org/10.1146/annurev.earth.26.1.111.

Magee, J. W., G. H. Miller, N. A. Spooner, and D. Questiaux, 2004: Continuous 150 ky monsoon record from Lake Eyre, Australia: Insolation-forcing implications and unexpected Holocene failure. *Geology*, **32**, 885–888, https://doi.org/10.1130/G20672.1.

Marchant, R., C. Mumbi, S. Behera, and T. Yamagata, 2007: The Indian Ocean dipole—The unsung driver of climatic variability in East Africa. *Afr. J. Ecol.*, **45**, 4–16, https://doi.org/10.1111/j.1365-2028.2006.00707.x.

Marengo, J., and Coauthors, 2012: Recent developments on the South American monsoon system. *Int. J. Climatol.*, **32**, 1–21, https://doi.org/10.1002/joc.2254.

McGowan, H., S. Marx, P. Moss, and A. Hammond, 2012: Evidence of ENSO mega-drought triggered collapse of prehistory Aboriginal society in northwest Australia. *Geophys. Res. Lett.*, **39**, L22702, https://doi.org/10.1029/2012GL053916.

Meehl, G., J. Arblaster, J. Caron, H. Annamalai, M. Jochum, A. Chakraborty, and R. Murtugudde, 2012: Monsoon regimes and processes in CCSM4. Part I: The Asian–Australian monsoon. *J. Climate*, **25**, 2583–2608, https://doi.org/10.1175/JCLI-D-11-00184.1.

Merlis, T., T. Schneider, S. Bordoni, and I. Eisenman, 2013: Hadley circulation response to orbital precession. Part I: Aquaplanets. *J. Climate*, **26**, 740–753, https://doi.org/10.1175/JCLI-D-11-00716.1.

Mizuta, R., and Coauthors, 2012: Climate simulations using MRI-AGCM3. 2 with 20-km grid. *J. Meteor. Soc. Japan*, **90A**, 233–258, https://doi.org/10.2151/jmsj.2012-A12.

Mohtadi, M., D. W. Oppo, S. Steinke, J.-B. W. Stuut, R. De Pol-Holz, D. Hebbeln, and A. Lückge, 2011: Glacial to Holocene swings of the Australian–Indonesian monsoon. *Nat. Geosci.*, **4**, 540–544, https://doi.org/10.1038/ngeo1209.

——, M. Prange, and S. Steinke, 2016: Palaeoclimatic insights into forcing and response of monsoon rainfall. *Nature*, **533**, 191–199, https://doi.org/10.1038/nature17450.

Moise, A., R. Colman, and J. Brown, 2012: Behind uncertainties in projections of Australian tropical climate: Analysis of 19 CMIP3 models. *J. Geophys. Res.*, **117**, D10103, https://doi.org/10.1029/2011JD017365.

Muller, C., and P. A. O'Gorman, 2011: An energetic perspective on the regional response of precipitation to climate change. *Nat. Climate Change*, **1**, 266–271, https://doi.org/10.1038/nclimate1169.

Neelin, J., and I. Held, 1987: Modeling tropical convergence based on the moist static energy budget. *Mon. Wea. Rev.*, **115**, 3–12, https://doi.org/10.1175/1520-0493(1987)115<0003:MTCBOT>2.0.CO;2.

Nguyen, H., H. Hendon, E.-P. Lim, G. Boschat, E. Maloney, and B. Timbal, 2018: Variability of the extent of the Hadley circulation in the Southern Hemisphere: A regional perspective. *Climate Dyn.*, **50**, 129–142, https://doi.org/10.1007/s00382-017-3592-2.

Nieto-Ferreira, R., T. M. Rickenbach, and E. A. Wright, 2011: The role of cold fronts in the onset of the monsoon season in the South Atlantic convergence zone. *Quart. J. Roy. Meteor. Soc.*, **137**, 908–922, https://doi.org/10.1002/qj.810.

O'Gorman, P. A., R. P. Allan, M. P. Byrne, and M. Previdi, 2012: Energetic constraints on precipitation under climate change. *Surv. Geophys.*, **33**, 585–608, https://doi.org/10.1007/s10712-011-9159-6.

Ohgaito, R., and A. Abe-Ouchi, 2007: The role of ocean thermodynamics and dynamics in Asian summer monsoon changes during the mid-Holocene. *Climate Dyn.*, **29**, 39–50, https://doi.org/10.1007/s00382-006-0217-6.

Oueslati, B., S. Bony, C. Risi, and J.-L. Dufresne, 2016: Interpreting the inter-model spread in regional precipitation projections in the tropics: Role of surface evaporation and cloud radiative effects. *Climate Dyn.*, **47**, 2801–2815, https://doi.org/10.1007/s00382-016-2998-6.

Pascale, S., L. M. Carvalho, D. K. Adams, C. L. Castro, and I. F. Cavalcanti, 2019: Current and future variations of the monsoons of the Americas in a warming climate. *Curr. Climate Change Rep.*, **5**, 125–144, https://doi.org/10.1007/s40641-019-00135-w.

Raia, A., and I. F. A. Cavalcanti, 2008: The life cycle of the South American monsoon system. *J. Climate*, **21**, 6227–6246, https://doi.org/10.1175/2008JCLI2249.1.

Rowe, C., 2007: A palynological investigation of Holocene vegetation change in Torres Strait, seasonal tropics of northern Australia. *Palaeogeogr. Palaeoclimatol. Palaeoecol.*, **251**, 83–103, https://doi.org/10.1016/j.palaeo.2007.02.019.

Schefuß, E., S. Schouten, and R. R. Schneider, 2005: Climatic controls on central African hydrology during the past 20,000 years. *Nature*, **437**, 1003–1006, https://doi.org/10.1038/nature03945.

Schneider, T., T. Bischoff, and G. H. Haug, 2014: Migrations and dynamics of the intertropical convergence zone. *Nature*, **513**, 45–53, https://doi.org/10.1038/nature13636.

Schulz, H., U. von Rad, and H. Erlenkeuser, 1998: Correlation between Arabian Sea and Greenland climate oscillations of the past 110,000 years. *Nature*, **393**, 54–57, https://doi.org/10.1038/31750.

Schwendike, J., G. J. Berry, M. J. Reeder, C. Jakob, P. Govekar, and R. Wardle, 2015: Trends in the local Hadley and local Walker circulations. *J. Geophys. Res. Atmos.*, **120**, 7599–7618, https://doi.org/10.1002/2014JD022652.

Seager, R., N. Harnik, Y. Kushnir, W. Robinson, and J. Miller, 2003: Mechanisms of hemispherically symmetric climate variability. *J. Climate*, **16**, 2960–2978, https://doi.org/10.1175/1520-0442(2003)016<2960:MOHSCV>2.0.CO;2.

——, N. Naik, and G. A. Vecchi, 2010: Thermodynamic and dynamic mechanisms for large-scale changes in the hydrological cycle in response to global warming. *J. Climate*, **23**, 4651–4668, https://doi.org/10.1175/2010JCLI3655.1.

Seth, A., M. Rojas, and S. A. Rauscher, 2010: CMIP3 projected changes in the annual cycle of the South American monsoon. *Climatic Change*, **98**, 331–357, https://doi.org/10.1007/s10584-009-9736-6.

——, S. A. Rauscher, M. Rojas, A. Giannini, and S. J. Camargo, 2011: Enhanced spring convective barrier for monsoons in a warmer world? *Climatic Change*, **104**, 403–414, https://doi.org/10.1007/s10584-010-9973-8.

——, ——, M. Biasutti, A. Giannini, S. J. Camargo, and M. Rojas, 2013: CMIP5 projected changes in the annual cycle of precipitation in monsoon regions. *J. Climate*, **26**, 7328–7351, https://doi.org/10.1175/JCLI-D-12-00726.1.

Shongwe, M. E., G. J. van Oldenborgh, B. van den Hurk, and M. van Aalst, 2011: Projected changes in mean and extreme precipitation in Africa under global warming. Part II: East Africa. *J. Climate*, **24**, 3718–3733, https://doi.org/10.1175/2010JCLI2883.1.

Shulmeister, J., 1999: Australasian evidence for mid-Holocene climate change implies precessional control of Walker circulation in the Pacific. *Quat. Int.*, **57-58**, 81–91, https://doi.org/10.1016/S1040-6182(98)00052-4.

Simon, M. H., M. Ziegler, J. Bosmans, S. Barker, C. J. Reason, and I. R. Hall, 2015: Eastern South African hydroclimate over the past 270,000 years. *Sci. Rep.*, **5**, 18153, https://doi.org/10.1038/srep18153.

Smith, R. J., and F. E. Mayle, 2018: Impact of mid-to late Holocene precipitation changes on vegetation across lowland tropical South America: A paleodata synthesis. *Quat. Res.*, **89**, 134–155, https://doi.org/10.1017/qua.2017.89.

Sperber, K., H. Annamalai, I. Kang, A. Kitoh, A. Moise, A. Turner, B. Wang, and T. Zhou, 2013: The Asian summer monsoon: An intercomparison of CMIP5 vs. CMIP3 simulations of the late 20th century. *Climate Dyn.*, **41**, 2711–2744, https://doi.org/10.1007/s00382-012-1607-6.

Stocker, T. F., and Coauthors, 2014: *Climate Change 2013: The Physical Science Basis*. Cambridge University Press, 1535 pp.,https://doi.org/10.1017/CBO9781107415324.

Su, H., and J. D. Neelin, 2005: Dynamical mechanisms for African monsoon changes during the mid-Holocene. *J. Geophys. Res.*, **110**, D19105, https://doi.org/10.1029/2005JD005806.

Tian, Z., T. Li, and D. Jiang, 2018: Strengthening and westward shift of the tropical Pacific Walker circulation during the mid-Holocene: PMIP simulation results. *J. Climate*, **31**, 2283–2298, https://doi.org/10.1175/JCLI-D-16-0744.1.

Tierney, J. E., and F. S. Pausata, 2017: Rainfall regimes of the Green Sahara. *Sci. Adv.*, **3**, e1601503, https://doi.org/10.1126/sciadv.1601503.

——, J. M. Russell, Y. Huang, J. S. S. Damsté, E. C. Hopmans, and A. S. Cohen, 2008: Northern Hemisphere controls on tropical southeast African climate during the past 60,000 years. *Science*, **322**, 252–255, https://doi.org/10.1126/science.1160485.

Tjallingii, R., M. Claussen, J.-B. W. Stuut, J. Fohlmeister, A. Jahn, T. Bickert, F. Lamy, and U. Röhl, 2008: Coherent high- and low-latitude control of the northwest African hydrological balance. *Nat. Geosci.*, **1**, 670–675, https://doi.org/10.1038/ngeo289.

Trenberth, K. E., and C. J. Guillemot, 1995: Evaluation of the global atmospheric moisture budget as seen from analyses. *J. Climate*, **8**, 2255–2272, https://doi.org/10.1175/1520-0442(1995)008<2255:EOTGAM>2.0.CO;2.

Vecchi, G. A., and B. J. Soden, 2007: Global warming and the weakening of the tropical circulation. *J. Climate*, **20**, 4316–4340, https://doi.org/10.1175/JCLI4258.1.

Walker, J., 2017: Seasonal and interannual variability in South Asian monsoon dynamics. Ph.D. thesis, California Institute of Technology, 121 pp.

Wang, X., and Coauthors, 2017: Hydroclimate changes across the Amazon lowlands over the past 45,000 years. *Nature*, **541**, 204–207, https://doi.org/10.1038/nature20787.

Wang, Y., and Coauthors, 2008: Millennial and orbital-scale changes in the East Asian monsoon over the past 224,000 years. *Nature*, **451**, 1090–1093, https://doi.org/10.1038/nature06692.

Ward, B. M., and Coauthors, 2019: Reconstruction of Holocene coupling between the South American monsoon system and local moisture variability from speleothem δ18O and 87Sr/86Sr records. *Quat. Sci. Rev.*, **210**, 51–63, https://doi.org/10.1016/j.quascirev.2019.02.019.

Webster, P. J., and S. Yang, 1992: Monsoon and ENSO: Selectively interactive systems. *Quart. J. Roy. Meteor. Soc.*, **118**, 877–926, https://doi.org/10.1002/qj.49711850705.

Weldeab, S., D. W. Lea, R. R. Schneider, and N. Andersen, 2007: 155,000 years of West African monsoon and ocean thermal evolution. *Science*, **316**, 1303–1307, https://doi.org/10.1126/science.1140461.

Yu, B., and F. W. Zwiers, 2010: Changes in equatorial atmospheric zonal circulations in recent decades. *Geophys. Res. Lett.*, **37**, L05701, https://doi.org/10.1029/2009GL042071.

Yuan, D., and Coauthors, 2004: Timing, duration, and transitions of the last interglacial Asian monsoon. *Science*, **304**, 575–578, https://doi.org/10.1126/science.1091220.

Zhao, Y., and S. Harrison, 2012: Mid-Holocene monsoons: A multi-model analysis of the inter-hemispheric differences in the responses to orbital forcing and ocean feedbacks. *Climate Dyn.*, **39**, 1457–1487, https://doi.org/10.1007/s00382-011-1193-z.

——, and Coauthors, 2005: A multi-model analysis of the role of the ocean on the African and Indian monsoon during the mid-Holocene. *Climate Dyn.*, **25**, 777–800, https://doi.org/10.1007/s00382-005-0075-7.

Zhou, T., L. Zhang, and H. Li, 2008: Changes in global land monsoon area and total rainfall accumulation over the last half century. *Geophys. Res. Lett.*, **35**, L16707, https://doi.org/10.1029/2008GL034881.